C2SMART
CONNECTED CITIES WITH SMART TRANSPORTATION
A USDOT University Transportation Center

New York University
Rutgers University
University of Washington
University of Texas at El Paso
The City College of New York

Quantifying Uncertainty and Distributed Control for Unanticipated Traffic Patterns as a Result of Natural and Man-Made Disruptions

September 2018

C2SMART Center is a USDOT Tier 1 University Transportation Center taking on some of today's most pressing urban mobility challenges. Using cities as living laboratories, the center examines transportation problems and field tests novel solutions that draw on unprecedented recent advances in communication and smart technologies. Its research activities are focused on three key areas: Urban Mobility and Connected Citizens; Urban Analytics for Smart Cities; and Resilient, Secure, and Smart Transportation Infrastructure.

Some of the key areas C2SMART is focusing on include:

Disruptive Technologies

We are developing innovative solutions that focus on emerging disruptive technologies and their impacts on transportation systems. Our aim is to accelerate technology transfer from the research phase to the real world.

Unconventional Big Data Applications

C2SMART is working to make it possible to safely share data from field tests and non-traditional sensing technologies so that decision-makers can address a wide range of urban mobility problems with the best information available to them.

Impactful Engagement

The center aims to overcome institutional barriers to innovation and hear and meet the needs of city and state stakeholders, including government agencies, policy makers, the private sector, non-profit organizations, and entrepreneurs.

Forward-thinking Training and Development

As an academic institution, we are dedicated to training the workforce of tomorrow to deal with new mobility problems in ways that are not covered in existing transportation curricula.

Led by the New York University Tandon School of Engineering, C2SMART is a consortium of five leading research universities, including Rutgers University, University of Washington, University of Texas at El Paso, and The City College of New York.

c2smart.engineering.nyu.edu

Quantifying Uncertainty and Distributed Adaptive Control For Unanticipated Traffic

Saif Jabari
New York University Abu Dhabi

DianChao Lin
New York University

Li Li
New York University

Bilal Thonnam Thodi
New York University Abu Dhabi

Disclaimer

The contents of this report reflect the views of the authors, who are responsible for the facts and the accuracy of the information presented herein. This document is disseminated in the interest of information exchange. The report is funded, partially or entirely, by a grant from the U.S. Department of Transportation's University Transportation Centers Program. However, the U.S. Government assumes no liability for the contents or use thereof.

Acknowledgements

We wish to acknowledge the Abu Dhabi Department of Transportation for their support, specifically with help identifying a congested urban corridor in the city and for providing traffic data. We also wish to acknowledge Timothy Mulumba for his assistance with preparing the microsimulation testbed. We also wish to acknowledge Professor Fangfang Zheng of Southwest Jiaotong University for help with developing and testing our estimation techniques using stochastic Lagrangian modeling.

Executive Summary

Non-recurring traffic congestion, in the form of traffic incidents, accounts for over 50% of day-to-day traffic delays. We are also seeing an increasing frequency of other major traffic disruptions, both anticipated (e.g., hurricanes) and no-notice (e.g., man-made disasters). Changes in traffic patterns under such conditions render existing control strategies, which are typically optimized to handle "typical" traffic conditions, obsolete. In fact, these control strategies can even contribute to worsening traffic conditions.

As new sources of traffic and related data are becoming more widely available and at a granularity that was inconceivable only a decade ago, our ability to measure traffic conditions and detect incidents has dramatically improved. Responding to such conditions in real-time via control strategies that are tailored to the nature of the incident is a natural next step in the process. But performing optimal control calculations in real-time and in a way that captures (i) uncertainties in the evolution of traffic conditions and (ii) queue build-up and dissipation dynamics in a network setting cannot be achieved with present state-of-the-art algorithms.

This report presents real-time distributed network control techniques capable of utilizing various types of real-time traffic data, from both fixed and mobile sources. The work is divided into two major parts: traffic state estimation when data is limited and adaptive control. The first part develops techniques that produce data needed for the control techniques developed in the second part of this report. Stochastic model of traffic flow for modeling uncertainty in traffic conditions are first developed and then state estimation techniques that aim at imputing traffic data spatially are developed and tested. Project background and literature reviews are given in Section 1, which is followed by a description of the network model developed for testing purposes in Section 2.

Two methodologies for traffic state estimation are presented in Section 3: (i) A conditional random fields (CRF) approach that combines mesoscopic traffic modeling with the statistical power of probabilistic graphical models to learn the traffic patterns from historical data, including both look-ahead dynamics along with vehicle interaction dynamics, and (ii) a stochastic Lagrangian model utilizing the Newell-Franklin equilibrium relation along with a second-order Gaussian approximation are developed. The latter allows for fast estimation techniques to be used (namely, standard Kalman filters). For the CRF approach, we use a factor graph representation of the mesoscopic dynamics, which is a graphical tool that helps simplify the estimation process. Coverage of the probe vehicle information can be expected to be highly random as well as sparse in the real-world. The experiments demonstrate that the distribution

of probes in a sample can severely impact the estimation results, and hence it is not sufficient to specify adequate penetration levels with a single value.

A new Backpressure (BP) algorithm tailored to traffic dynamics (namely, capturing queue build-up and dissipation) is developed in Section 4. The proposed approach overcomes drawbacks in the original theory from a traffic dynamics point of view, specifically, infinite arc capacities, point queues, independence of commodities (turning movements), and there being no analogue for start-up lost times in communications networks (where BP was originally developed). These are critical features in intersection control. The backpressure control technique developed in this report is based on macroscopic traffic flow and is referred to as *position-weighted backpressure* (PWBP).

Fourthly, we use real world data to test the effects of traffic state estimation and network control in Section 5.1. The NGSIM trajectory data along I-80 in the San Francisco Bay area in Emeryville, CA is used. The traffic state in terms of density dynamics can be well estimated with 10% penetration rate. The investigation of the speed estimation error in terms of RMSEs for different penetration rates illustrate that there is strong improvement as the penetration rates increase from 5% to 15%. Additionally, a microscopic traffic simulation model of an eleven-intersection network in Abu Dhabi is used to test the proposed PWBP control policy in Section 5.2. Comparisons against coordinated and optimized fixed signal timing, standard BP, and a capacity-aware variant of BP (CABP) were carried out. The results indicate that PWBP can accommodate higher demand levels than the other three control policies and outperforms them in terms of total network delay, congestion propagation speed, recoverability from heavy congestion, and response to an incident.

Table of Contents

List of Figures

List of Tables

1 Introduction

1.1 Background and Literature Review

Automated vehicle (AV) technologies are beginning to penetrate vehicle fleets in cities throughout the world. It is reasonable to expect that vehicle trajectory data from AVs (e.g., through on-board GPS units) will become a prominent source of high-resolution traffic data. AVs may act as probes in the traffic stream, continuously broadcasting their position and speed in real-time. More importantly, AVs can also provide distance headways (spacing between successive vehicles) using infrared or radio technology [1, 2]. However, privacy issues and technology limitations can limit the ability of traffic management agencies to collect, analyze, and disseminate such information. To overcome this, these data can be fused with data obtained from traditional monitoring devices such as inductive-loop detectors (stationary sensors). As these two data sources complement each other, comprehensive datasets can be obtained for traffic monitoring and state estimation [3]. However, the improvement in accuracy with data fusion over single sensor applications depends on probe penetration rates and on traffic conditions. In urban road networks, where stationary sensor instrumentation is usually limited and traffic lights play a governing role in the traffic dynamics, a higher number of probes may be necessary to accurately characterize traffic conditions.

A number of modeling techniques have been proposed in recent years to estimate traffic densities [4, 5, 6, 7], speeds [8] and travel times [9, 10]. Studies have also been carried out to extract patterns from streaming data using data mining techniques [11, 12, 13, 14]. To account for the variability in urban traffic, statistical approaches using Coupled Hidden Markov Models were also applied to estimate the traffic state from sparse probe data [15]. Hybrid modeling tools that combine machine learning with hydrodynamic traffic theory have also been applied to predict arterial travel times from streaming GPS probe data, [16] and data-driven modeling to capture longitudinal interactions between vehicles has also been investigated [17].

Research on traffic state estimation from probe data for urban networks has focused on the reconstruction of traffic states at an aggregate level (over an entire intersection-to-intersection road segment) [18]. At a finer scale, traffic densities on a freeway section are reconstructed by modifying traditional continuum models with a correction term to nudge the model estimate towards the GPS probe measurements [4]. The maximum sampling interval (time between two consecutive probe vehicle samples) required to accurately detect incidents and the optimal

placement of sensors for reliable time-to-detection of incidents have also been studied [19, 20]. Comparisons of travel time estimates produced using one source of data versus fused data from two data sources (stationary sensors and probe vehicle data) were performed by Mazaré et al. [21] and a number of studies have reported probe penetration rates required for traffic state estimation on arterials [22, 23, 24, 25]. While the reliability of probe vehicle data has been investigated and compared against stationary sensor data [26, 27], variability in the spatio-temporal coverage of probe vehicles has not been adequately studied, particularly at the fine level required for effective traffic management.

Motivated by the wide spatio-temporal coverage offered by fused traffic data, the question of adequate levels of probe penetration is addressed at a microscopic scale in this research. The focus of the random fields estimation part of this research is on the reconstruction of vehicle trajectories over a single roadway, where a stationary sensor captures the arrival times of the vehicles and the speeds of the probe vehicles is used to infer the traffic state over the entire link. A probabilistic approach is proposed for the spatio-temporal reconstruction of dynamic traffic state from sparse probe data, wherein the traffic patterns are learned from historical data using Conditional Random Fields (CRFs). By modeling the vehicle interaction potential to reflect local traffic information (such as spacings between vehicles), our estimation models seamlessly combine traditional car-following theory and simulation with statistical learning techniques to reconstruct microscopic traffic dynamics.

1.2 Traffic estimation with Lagrangian measurements

Another class of traffic estimation techniques build on the Lighthill, Whitham, and Richards traffic flow model [28, 29] (the LWR model). These approaches are formulated using traditional spatial-temporal (Eulerian) coordinates and are most suitable for state estimation with point sensor measurements (macroscopic data, e.g., traffic volume, speeds). Data from probe vehicles or connected vehicles (microscopic data, e.g., vehicle trajectories) are becoming increasingly available. Traffic flow models that are able to effectively utilize such data are of greater interest in modern applications. A simple way of interfacing between the microscopic and the macroscopic worlds is via coordinate transformations. Indeed, this was done by Daganzo [30, 31] and later extended by Leclercq et al. [32] . The former proposes a variational formulation of the LWR model in Eulerian coordinates, while the latter formulate the model in Lagrangian coordinates. More recently, Hamilton-Jacobi based formulations of traffic flow have

appeared in the literature, [33, 34] and some researchers applied the theory to formulate first-order models in three different coordinate systems [35], namely the traditional Eulerian coordinates and two variants of Lagrangian coordinates. Proposed solutions schemes for the deterministic Lagrangian models include both variational techniques and the Godunov scheme using a triangular fundamental diagram. Specifically, the Godunov scheme in Lagrangian coordinates simplifies to an upwind scheme, enabling more efficient application of data assimilation methods [1, 35, 36].

Though deterministic traffic flow models and their solution methods have been extensively studied in the literature, stochastic models of traffic flow are still in a burgeoning stage of development and are primarily extensions of existing deterministic models. For example, stochastic extensions of the cell transmission model [37, 38] have been proposed [5,39]; other approaches have extended the link transmission model [40], both at the individual link level and the network level [41, 42, 43, 44]. In general, there still remain issues related to the physical accuracy of the sample paths of existing stochastic traffic models, particularly those developed for purposes of traffic state estimation (see references [45,46] for recent reviews). The main culprit is the dominance of time-stochasticity (or noise) in the stochastic models, mostly developed in Eulerian coordinates [6, 8, 39, 47, 48, 49, 50, 51, 52, 53, 54, 55], but also in Lagrangian coordinates[1, 56, 57]. This results in sample paths prone to aggressive oscillation in the time dimension. The interpretation of these oscillations is (unreasonably) aggressive acceleration and deceleration dynamics.

This report addresses the physical relevance issue of stochastic traffic dynamics via a new stochastic Lagrangian model of traffic flow. The source of uncertainty is parametric in the same sense proposed by Jabari et al. [58]. The interpretation of this form of uncertainty is heterogeneity in the driving population. A stochastic version of Newell-Franklin speed spacing relation [59, 60] is utilized. Unlike Newell's simplified relation [61], a unique inverse function exists, which can be used in data assimilation applications. Using parametric uncertainty, the sample paths of the stochastic process are smooth and do not contain the oscillatory behavior above. The Lagrangian estimation technique in this research focuses on application of the proposed model (using parametric uncertainty) for traffic state estimation (TSE), which is a precursor to a variety of traffic management applications, specifically control applications. TSE is particularly crucial when data availability is limited. Non-linearity of traffic models renders the TSE particularly challenging. In theory, one utilizes sampling techniques (e.g., ensemble filters,

particle filter, etc.). These approaches are time consuming and cannot be applied in real-time. To address this issue, the mean and covariance dynamics are derived in a way that preserves the dependencies (i.e., richness) in the model, while allowing for use of standard Kalman filtering techniques. The latter are known to be computationally tractable and amenable to real-time applications.

1.3 Position-weighted backpressure control

Various approaches have been proposed to optimize signal timing for isolated intersections, including mixed-integer linear models, rolling horizon approaches, and store-and-forward models based on model predictive control [62, 63, 64, 65, 66, 67]. On the one hand, isolated intersection approaches fail to account for spillback from adjacent road segments, which can eventually lead to gridlock throughout a road network [68]. On the other hand, centralized techniques that include coordination between intersection controllers [69, 70] are not scalable and difficult to implement in real-world/real-time settings [71]. For example, ACS-Lite [70] can handle no more than 12 intersections in real-time.

Decentralized control techniques have been proposed to overcome the scalability issues associated with network control optimization. These techniques expect intersection controllers to be able to measure/estimate local traffic information in real-time. This information includes expected traffic demand at the intersection in the next cycle for heuristic approaches [72, 73, 74, 75], or the queue sizes along the intersection arcs in max pressure based approaches [76, 77, 78, 79]. According to De Gier et al. [80], control strategies that use traffic conditions along both upstream and downstream arcs are more efficient and reliable than those that utilize upstream traffic conditions only. Recently, backpressure (BP) control techniques have been adopted to signal control; they were first independently proposed by Wongpiromsarn et al. and Varaiya [76, 77] based on seminal work in communications networks [81, 82, 83, 84]. In general, BP based approaches are scalable and come with theoretical guarantees of network stability. However, as it was originally developed for packet queueing in communications networks, the assumptions are not tailored to traffic problems and in some cases the assumptions are not suitable for traffic networks. Specifically, these models assume point queues and (more critically) infinite queue size capacity. As a result, the models do not account for the spatial distribution of the queues and (more importantly) cannot account for spillback. Another drawback is loss of work conservation, in which no flow is allowed (all red) despite the

availability of capacity in the outbound arcs. For example, Figure 1-1 shows three cases in which BP control favors the eastbound approach (Q_a to Q_b), even though no vehicles could actually pass the intersection from this approach. Recognizing this problem, some researchers proposed an improvement, referred to as *capacity aware back pressure* (CABP) control [85]. Their approach can avoid the case illustrated in Figure 1-1a, but not the two depicted in Figure 1-1b and Figure 1-1c (in the former, the queue is concentrated at the ingress of the arc). This is due to the fact that their approach models traffic as a point queue.

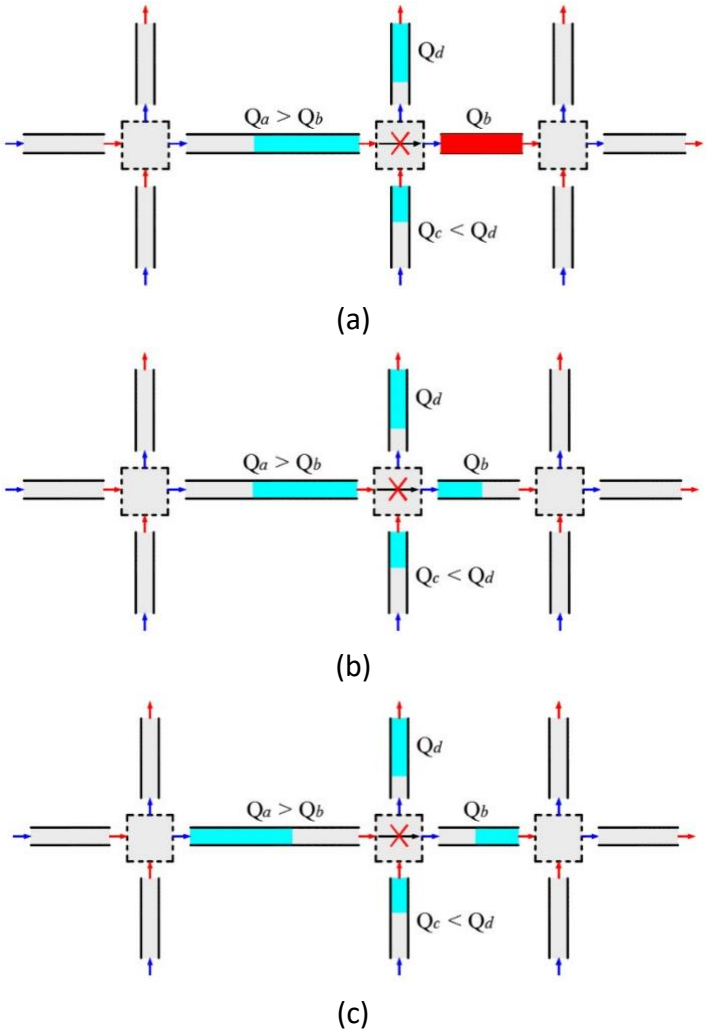

Figure 1-1 Three non-work conserving cases (adopted [85] and reproduced)

Another feature of the dynamics of communications networks that does not apply to (road) traffic networks is separate queues for different commodities (corresponding to vehicles with different turning desires in traffic) and no interference between commodities. Shared lanes, which are very common, are one example where this assumption is violated in traffic networks. Even when there are no shared lanes, road widening near the egress's intersection inbound

arcs, also very common geometrical features in urban networks, can create bottlenecks at the lane-branching point. Different turning movements (commodities) interact at the bottleneck, and one queue may block another if it gets too long, as illustrated in Figure 1-2. In (road) traffic networks, one has to consider start-up and clearance lost times (i.e. the green lost time) and avoid frequent phase switching. These features do not exist in communications networks and existing BP control approach applied to traffic flow has not considered such green lost time.

The traffic control part of this research proposes decentralized intersection control techniques that build upon macroscopic traffic theory and overcome the issues described above. This approach is referred to as *position-weighted backpressure* (PWBP). PWBP considers the spatial distribution of vehicles along the road, applying higher weights to queues that extend to the ingress of the road, thereby accounting for the possibility of spillback. Flow rates entering the intersection depend on both the control and the traffic density, thereby capturing diminished flows at phase startups (startup lost times).

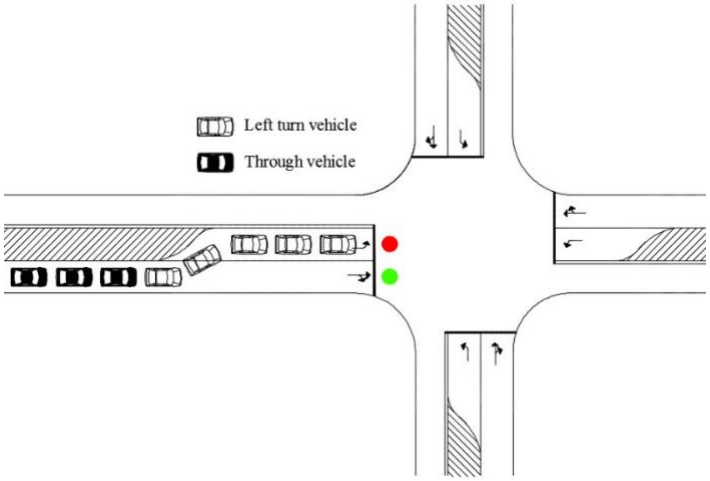

Figure 1-2 Bottleneck at the lane-branching point.

The type of control proposed can be applied to intersection signal control, i.e., today's traffic lights. But it can also be thought of as a prioritization scheme for connected vehicles at network intersections that can guarantee network stability. In both cases, when accurate measurement of the distribution of vehicles along the roads is not possible, one may employ a light-weight traffic state estimation technique, such as the Lagrangian TSE method presented in the sequel.

2 Network simulation and SCOOT emulator

2.1 Test network

The test network considered for simulation is an eleven-intersection network in Abu Dhabi, UAE, covering a 2 sq.km area. A google map view of the network – depicting its general topology – is shown in Figure 2-1. The network forms a part of Abu Dhabi downtown and is surrounded by a mix of residential and commercial establishments. As such, distinct peaking of traffic volumes along the major streets of the network can be observed during morning and evening times.

Figure 2-1 Layout of test network. Located in downtown Abu Dhabi, UAE. (www.maps.google.com)

The network has two major arterials (Fatima Bint Mubarak Street and Sheikh Zayed Bin Street) that run parallel to each other and is interconnected by four other major streets to form a regular grid shaped network. These arterials form the skeleton of the network. The major arterials are 3 to 4 lanes wide, with an exclusive left turn and right turn lane (of average length of 50m) at each incoming link near the intersection stop line. Major streets in the network, their names, and other general details on the streets are listed in Table 2-1. The minor streets in the network give access to residential and business offices from the major arterials. These minor streets are 1 or 2 lanes wide. There are at least two entries and exits from these major

arterials. The network has 11 major signalized intersections (details are given in Table 2-2 and Table 2-3). The traffic lights are operated by an adaptive controller (SCOOT [86] – an adaptive traffic signal controller, developed in the UK).

No.	Arterial/Street Name	Length	Number of lanes
1	Fatima Bint Mubarak St.	1.85 km	3 lanes
2	Sheikh Zayed Bin Sultan St.	1.75 km	4 lanes
3	Hamdan Bin Mohammed St.	1.10 km	3 lanes
4	Zayed The First St.	1.06 km	3 lanes
5	9th Street	0.96 km	3 lanes
6	Al Falah Street	0.60 km	4 lanes
7	19th Street	0.33 km	3 lanes
8	10th Street (vertical)	0.67 km	3 lanes

Table 2-1 Major arterial geometric details

No.	Intersection Name	Streets forming the intersection	
		In North-South direction	In West-East direction
1	IP 17	Fatima Bint Mubarak street	Hamdan Bin Mohammad street
2	IP 10	Fatima Bint Mubarak street	Zayed The First street
3	IP 11C	Fatima Bint Mubarak street	9th Street
4	IP 35	Fatima Bint Mubarak street	Al Falah street
5	IP 11B	10th street	9th street
6	IP 36B	10th street	Al Falah street
7	IP 9	Sheikh Zayed Bin Sultan street	Hamdan Bin Mohammad street
8	IP 11	Sheikh Zayed Bin Sultan street	Zayed The First street

9	IP 11A	Sheikh Zayed Bin Sultan street	9th street
10	IP 36A	Sheikh Zayed Bin Sultan street	19th street
11	IP 36	Sheikh Zayed Bin Sultan street	Al Falah street

Table 2-2 Major signalized intersections in the network

The testbed selected for microscopic traffic simulation is shown in Figure 2-2. As seen, only that part of the network marked with blue lines – representing major arterials, entries and exits points, and signalized intersection – is considered for simulation. Entrances and exits to minor streets in the network serve as sources and sinks in the network, but traffic along the minor streets is not part of the simulation model.

Sl. No.	Intersection ID	Number of Lanes (LT/UT – ST)				Storage Lane Length - for LT/UT (m)				Detector Location (m)			
		1st	2nd	3rd	4th	1st	2nd	3rd	4th	1st	2nd	3rd	4th
1	IP 17	1-3	1-3	1-3	1-3	77	70	80	75	134	182	196	217
2	IP 10	1-3	1-3	1-3	1-3	80	80	75	80	187	200	200	146
3	IP 11C	-	1-3	2-0	1-3	-	65	-	65	-	150	180	135
4	IP 35	2-4	1-3	2-4	1-3	75	75	65	75	158	157	169	158
5	IP 11B	1-3	2-0	1-3	-	75	-	85	-	166	99	175	-
6	IP 36B	1-4	-	1-4	2-0	130	-	85	-	150	150	150	-
7	IP 9	2-3	2-4	2-3	1-3	75	75	75	75	156	180	170	147
8	IP 11	1-3	2-4	1-3	2-4	120	80	80	80	165	200	122	222
9	IP 11A	1-3	2-4	1-3	2-4	85	80	80	80	170	200	160	180
10	IP 36A	-	1-4	3-0	2-4	-	85	75	85	-	175	150	247
11	IP 36	2-3	2-4	2-3	2-4	105	75	75	75	190	133	114	170

Table 2-3 Geometric details of the intersections

There is a total of 227 sources and sinks in the network – corresponding to an origin-destination matrix of dimension 110 x 117 – and it captures all traffic demand in the network.

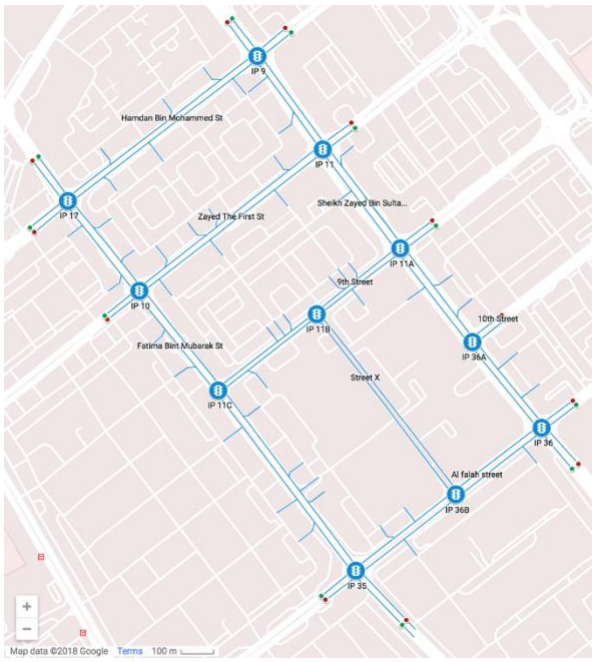

Figure 2-2 Simulation testbed of the calibrated network – showing only the major arterials, signalized intersections, and entries and exits, that will be simulated.

2.2 SCOOT emulator

The intersections in the network are controlled using the Split Cycle Offset Optimization Technique (SCOOT) adaptive controller. It optimizes cycle length, green splits, and offsets for a set of intersections, taking into account the prevailing traffic conditions in the network. This set of intersections, often related geographically, is referred to as a Region in the SCOOT literature; each region is controlled by a central controller.

Historical high resolution traffic data obtained from Abu Dhabi DOT [87] were utilized to develop a SCOOT emulator. The data utilized to train the emulator included data from the loop detectors (inputs to SCOOT) and signal status (output from SCOOT). The detector states were obtained at every quarter second and signal states were obtained at every one second. Signal states correspond to the status of each protected phase in the intersection. The emulator is essentially an Artificial Neural Network (ANN) [88,89]. This study used a Recurrent Neural Network (RNN) [90], which is widely used when the data has a sequential nature. In our case, the inputs are assumed to be a sequence of detector states at each previous time step, and the output is the signal states in the next time step. Also, we used a long short-term memory (LSTM) [91] instead of vanilla RNN to learn long term dependencies from the previous hidden

states. The structure of the recurrent neural network for the Scoot emulator is shown in Figure 2-3.

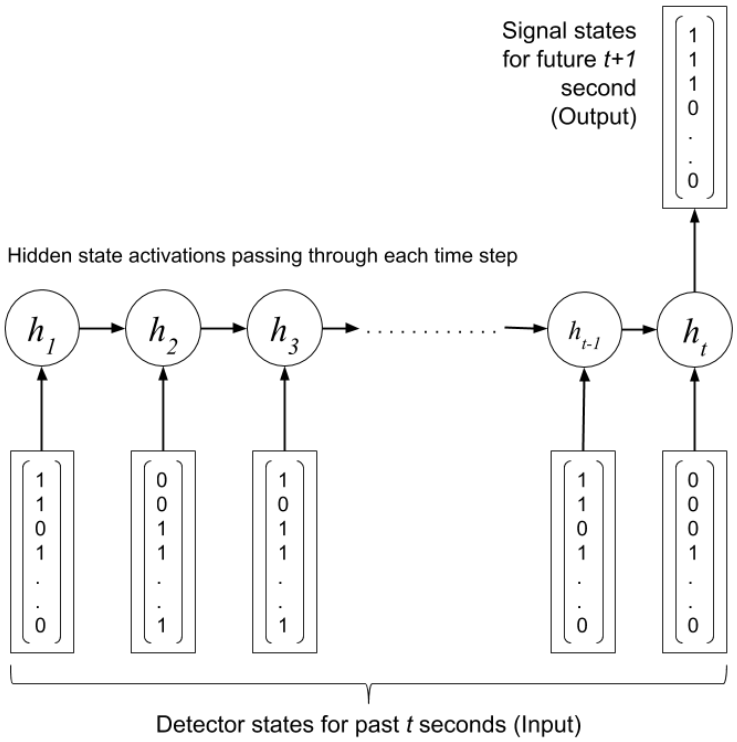

Figure 2-3 RNN architecture used for developing the emulator

The overall problem is structured as a classification problem: Given the detector states in the past *t* seconds, the neural network will predict the signal states, classed as either RED or GREEN, in the (*t*+1)th second. We divide the whole network into two regions and a separate neural network is built for each region. The first region contains the four intersections along the Fatima Bint Mubarak Street and the second region contains the remaining seven intersections. This partitioning captures the cycle length and signal coordination characteristics among the set of intersections operated by different controllers. The rationale for choosing a one-second prediction is that the neural network should also be able to learn the gap out characteristics based on real time vehicle actuations, from the data. The input-output characteristics, network architecture and learning parameters for the models of the two regions are detailed in Table 2-4. The models are trained using one day's data. The training of the neural network is done using Python [92] using the Tensorflow package [93] from Google. The python code is attached with the report (Scoot_emulator_rnn_training.py).

	Region 1	Region 2
Input-Output characteristics		
a) Number of intersections	4	7
b) Intersection IDs	17, 10, 11C, 35	11B, 36B, 9, 11, 11A, 36A, 36
c) Number of detectors	29	48
d) Number of signal heads	59	107
Network architecture		
e) Number of input nodes	29	48
f) Number of output nodes	59	107
g) Number of hidden layers	1	1
h) Number of hidden nodes in each layer	64	90
Learning parameters		
i) Learning rate	0.001	0.001
j) Loss function	Cross entropy	Cross entropy
k) Batch size	1000	1000
l) Number of iterations	400	400
m) Regularization (if any)	No	No

Table 2-4 Input/output characteristics, network architecture and learning parameters of the neural network

The neural network model for the two regions is trained using one day's data, which contains over 80,000 observations. The performance results during training are shown in Figure 2-4. The trained models are then tested using data from three days: a typical work day, a typical holiday, and a day with special event (Eid-ul-fitr). This allows us to understand how well the trained model generalizes to varying traffic conditions and to data that was not used to train the model. The accuracy, defined as the number of correctly classified signal states, of the trained models on the test data is tabulated in Table 2-5. Figure 2-5 and Figure 2-6 show sample snapshots of the signal timings predicted using the neural net and the signal timings as observed in the field. We observe that (1) the emulator captures the phase sequences very well. (2) It captures the phase durations and phase lagging and leading phenomena. (3) It captures the signal timings though there are some breaks observed in the predicted signal

timings. Overall, the trained model replicates field observed data very well thus serves a reasonable tool for simulating SCOOT.

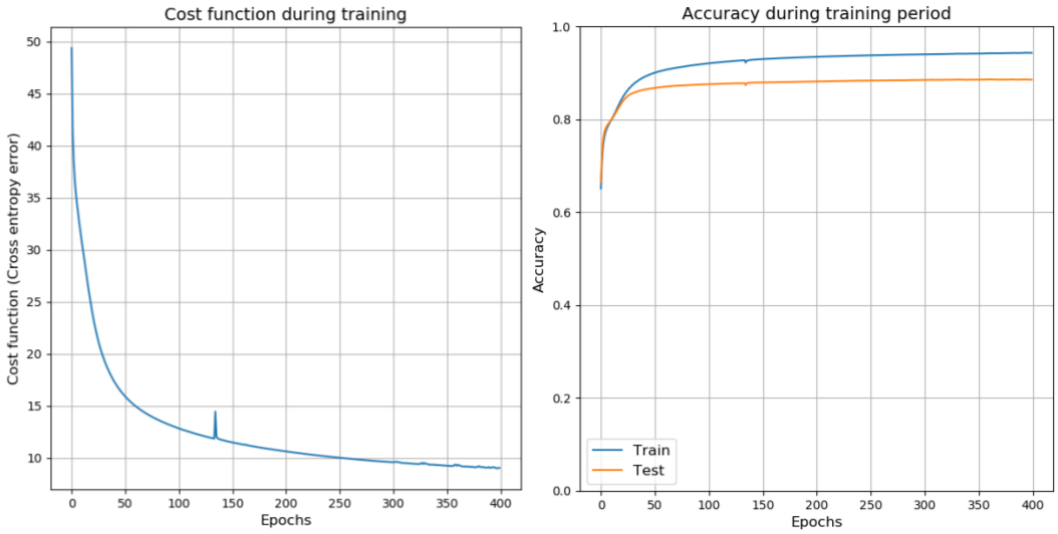

Figure 2-4 Performance of neural network during training for Region 1. (a) Cost function (b) Train and test accuracy

	Region 1 model	Region 2 model
Train data – 1 day	94.0 %	93.0 %
Test data – Typical working day.	92.5 %	90.9 %
Test data – Typical holiday.	92.0 %	88.1 %
Test data – A day with special event.	91.4 %	87.5 %

Table 2-5 Accuracy results

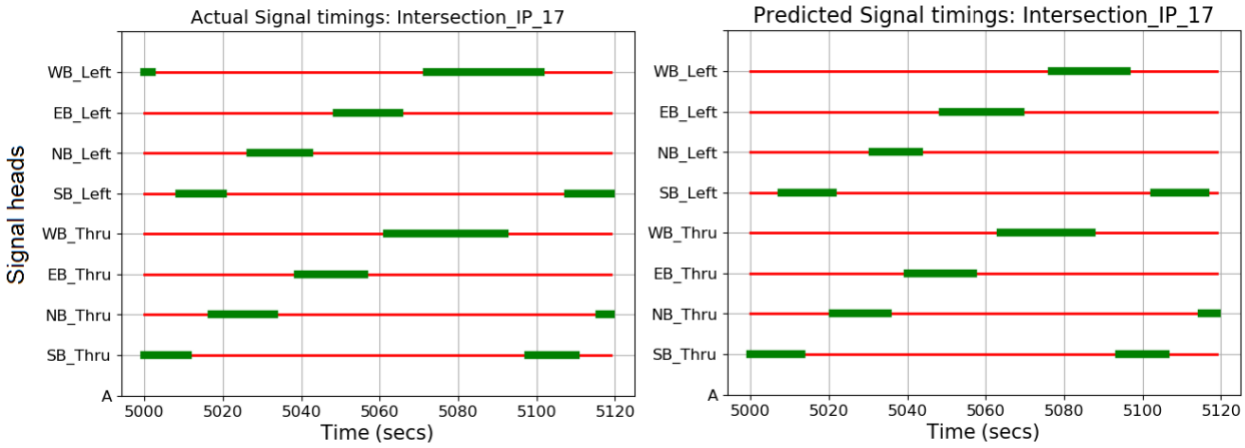

Figure 2-5 A snapshot of actual vs. predicted signal timings (Intersection IP17; Region 1)

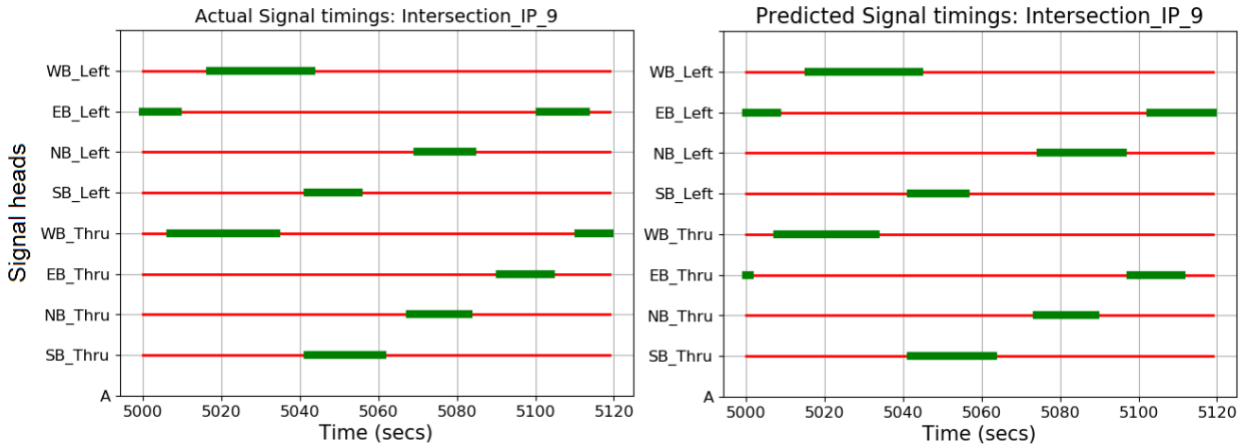

Figure 2-6 A snapshot of actual vs. predicted signal timings (Intersection IP9; Region 2)

2.3 Simulation of test network in microsimulation

VISSIM microscopic traffic simulator [94], from PTV Vision, is adopted to perform the simulation experiments. This study utilized a variety of sources of data to build and calibrate the network. The links, lane configurations, intersection layouts, etc., as described in 2.1 are used to code the network geometry; a snapshot is shown in Figure 2-7. The detectors, required for the working of SCOOT emulator, are positioned in accordance with what is found in the field. The control emulator is then implemented using VISSIM's COM interface [95]. The code for implementing the Scoot emulator in Vissim is attached with the document (Scoot_emulator_vissim_interface.py). Also, for comparison purposes, optimized fixed signal timing plans were developed using Synchro [96] (for different demand scenarios).

Figure 2-7 Test network

To check the performance of the emulator, we gradually increased the input traffic volume (Figure 2-8 Traffic demand) in the network (Region 1) and measured the signal timing and the cycle lengths predicted by the emulator. Figure 2-9 shows the signal cycle length observed at one of the intersections (IP 17) in Region 1. The trend line – with a positive slope – shows a commensurate increase in signal cycle length with traffic volume, signifying the emulator's ability to adapt to changing traffic demand.

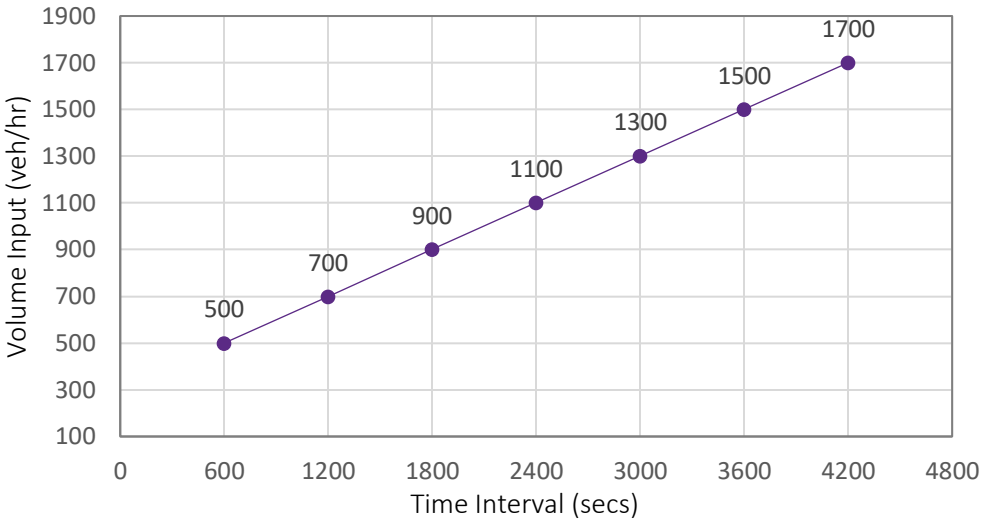

Figure 2-8 Traffic demands

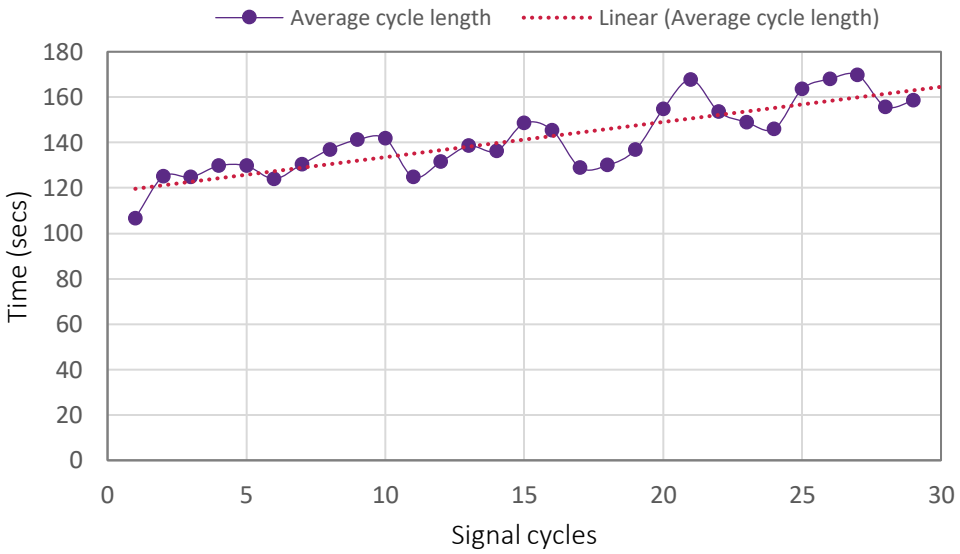

Figure 2-9 Cycle length observed using the emulator for intersection IP 17

3 Traffic state estimation

3.1 Learning Traffic Flow Dynamics using Random Fields

3.1.1 Stochastic Traffic Dynamics Model

Look-Ahead Dynamics

A discrete (state and time) mesoscopic stochastic model is used to represent the traffic dynamics. Vehicle movement in the model is governed by potential functions that describe the ("energy profile" of) local traffic conditions. Similar (but simpler) models have been employed to study interesting traffic phenomena like synchronized traffic at ramps and stop-and-go regimes [97].

The physical roadway is modeled as a one-dimensional uniform lattice L. The spatial co-ordinates of each vehicle α on the roadway is discretized in such a way that each cell can be occupied by at most one vehicle, which is achieved by setting the cell length to an appropriate value, e.g. 7.5 m [98]. The state of each occupied cell at a discrete time k is completely specified by a discretized speed denoted $v_k \in \{0, \ldots, v_{max}\}$, where v_{max} is the maximum number of cells that can be traversed by a vehicle in one time step. Clearly, v_{max} depends on the length of the discrete time step, δk. Thus, an order parameter $\sigma^k(l) \in \{-1, 0, \ldots, v_{max}\}$ can be defined for each cell $l \in L$ at time k to represent the traffic state in the cell, where 0 represents a free cell.

A look-ahead potential is used to capture the response of vehicle α to traffic conditions ahead. Specifically, the state of vehicle α at time-step $k + 1$ is a function of their current speed v_α^k and the current speed of their leader $v_{\alpha-1}^k$. Denote the traffic state pertaining to vehicle α at time step k by the vector $Y_\alpha^k = [v_\alpha^k \; v_{\alpha-1}^k]^{\mathrm{T}}$. More generally, a vehicle's look-ahead potential can depend on multiple vehicles ahead. Let M denote the look-ahead distance (in number of vehicles), then $Y_\alpha^k = [v_\alpha^k \; v_{\alpha-1}^k \; \ldots \; v_{\alpha-M}^k]^{\mathrm{T}}$. The look-ahead potential is given, for vehicle α and each $i \in \{0, \ldots, v_{max}\}$ by

$$\varepsilon_\alpha^k(i) = W_i^{\mathrm{T}} Y_\alpha^{k-1}, \tag{1}$$

where $W_i \in \mathrm{R}^{|Y|}$ is a weight vector that captures the relative importance of each of the state variables in Y_α^k when assessing the energy of vehicle α if it were to assume speed $i \in \{0, \ldots, v_{max}\}$. The parameters can, hence, be encoded into a matrix $W \in \mathrm{R}^{|Y| \times (v_{max}+1)}$ as $W \equiv [W_0 \ldots W_{v_{max}}]$.

Vehicle Interactions and Coordination

The modeling approach above is, in essence, a totally asymmetric simple exclusion process (TASEP). Such processes are known to have limitations in some contexts, namely, heterogeneous environments with AVs [99]. This is a result of vehicles reacting to the traffic conditions downstream. Introducing an interaction potential overcomes these limitations and offers enhanced interpretability to the probabilities of vehicles advancing to downstream cells [100]. Consider two interacting vehicles, *α* and *β* and let $Y^k_{\alpha,\beta}$ denote the traffic state pertaining the interaction between *α* and *β*. The interaction between *α* and *β* depends on distance between them and their speed difference: $Y^k_\alpha \equiv [g^k_{\alpha,\beta}\ \Delta v^k_{\alpha,\beta}]^{\mathrm{T}}$, where $g^k_{\alpha,\beta} = s^k_\alpha - s^k_\beta$ and $\Delta v^k_{\alpha,\beta} = v^k_\alpha - v^k_\beta$. For $i, j \in \{0, \ldots, v_{max}\}$, define the interaction potential as

$$\varepsilon^k_{\alpha,\beta}(i,j) \equiv \theta^{\mathrm{T}}_{i,j} Y^k_{\alpha,\beta}, \tag{2}$$

where $\theta_{i,j} \in \mathrm{R}^2$, is a vector of two parameters which represent the relative importance of each element in $Y^k_{\alpha,\beta}$ and $\varepsilon^k_{\alpha,\beta}(i,j)$ can be interpreted as the potential energy associated with vehicle *α* assuming speed *i* and vehicle *β* assuming speed *j* given their present state at time *k*.

The steps involved in simulating the traffic dynamics are summarized in Table 3-1 below, which without loss of generality assumes a free downstream boundary. This can be easily modified to accommodate downstream restrictions in a way that is similar to the upstream state update (see details on boundary treatments [101]).

Input:

No. lattice sites := *N*, No. time steps := *K* , time step := *δk*, max speed := v_{max}, Look-ahead distance := *M*, look-ahead matrix := *W*, interaction tensor := *Θ*, Arrival density := p_1, probability of Slow-down := p_2

Initialize:

Initial traffic state := $\sigma^0(I)$

Iterate:

For *k* = 1 : *K* **do**

For each *α*, set $Y^{k-1}_\alpha := [v^{k-1}_\alpha\ v^{k-1}_{\alpha\text{-}1} \ldots v^{k-1}_{\alpha\text{-}M}\ g^{k-1}_\alpha \ldots g^{k-1}_{\alpha-M+1}]^{\mathrm{T}}$

For each $\beta \neq \alpha$, set $Y^k_{\alpha,\beta} := [g^k_{\alpha,\beta}\ \Delta v^k_{\alpha,\beta}]^{\mathrm{T}}$

For $i \in \{0,\ldots,v_{max}\}$ **do**

Calculate the look-ahead potential $\varepsilon^k_\alpha(i) := W^{\mathrm{T}} Y^{k-1}_\alpha$

For $j \in \{0,\ldots,v_{max}\}$ **do**

Calculate the interaction potential $\varepsilon^k_{\alpha,\beta}(i,j) := \theta^{\mathrm{T}}_{i,j} Y^k_{\alpha,\beta}$

End For

End For

For each α **do**

Total potential $E_\alpha^k(i) := (v_{max}+1)\varepsilon_\alpha^k(i) + \sum_{j=0}^{v_{max}} \sum_{\alpha,\beta:\alpha\neq\beta} \varepsilon_{\alpha,\beta}^k(i,j)$

Probability $\pi_\alpha^k(i) := E_\alpha^k(i) / \sum_{i=0}^{v_{max}} \sum_{i=0}^{v_{max}} \left(\varepsilon_\alpha^k(i) + \sum_{\alpha,\beta:\alpha\neq\beta} \varepsilon_{\alpha,\beta}^k(i,j) \right)$

Velocity Update

Sample v_α^k from $[\pi_\alpha^k(1) \ldots \pi_\alpha^k(v_{max})]^T$

u_1 ~ Uniform(0, 1)

If $u_1 < p_2$ **then**

$v_\alpha^k = v_\alpha^k - 1$

End If

Position Update:

Compute vehicle positions s_α^k in ascending order of α:

If $s_\alpha^k := \min(s_\alpha^{k-1} + v_\alpha^k, s_{\alpha-1}^k - 1) > N$ **then**

$s_\alpha^k := \infty$

End If

Traffic State Update:

$\sigma^k(s_\alpha^k) = v_\alpha^k$

End For

Boundary Conditions:

u_2 ~ Uniform(0, 1)

If $u_2 < p_1$ and $\sigma^k(1) = 0$ **then**

$y := [v_{max} \; v_\alpha^k \; s_\alpha^k]^T$ (α is the index of upstream-most vehicle in the system)

For $i \in \{0, \ldots, v_{max}\}$, calculate $\hat{\pi}_i^k := \exp[-W_i^T y]$

and normalize: $\pi_i^k := \hat{\pi}_i^k / \sum_{i'=1}^{v_{max}} \hat{\pi}_{i'}^k$

$\sigma^k(1) \sim [\pi_1^k \; \ldots \; \pi_{v_{max}}^k]^T$

End If

End For

Table 3-1 Algorithm for simulation of traffic dynamics

3.1.2 Probabilistic Inference

Assume there are $|V|$ vehicles in the system and at each time step k, the state (speed and position) of a subset of these vehicles is observed. The estimation problem is concerned with determining the state of all vehicles given the partial observations. More accurately, the estimation problem seeks to fit the conditional probability distribution of the state given the

observations. Let $v=[i_1 \ldots i_{|V|}]^T$ and let $\pi_0(v) \equiv P(v_1^0=i_1,\ldots,v_{|V|}^0=i_{|V|})$, prior distribution of speeds (state at time 0), be given. Let $\sigma^{k,obs}$ denote the observed traffic states (measurements) available at time *k*. For each time step, the inference problem seeks to determine the conditional probability

$$\pi^k(i_1,\ldots,i_{|V|}) \equiv P(v_1^k=i_1,\ldots,v_{|V|}^0=i_{|V|}|\hat{Y}^{k-1},\sigma^{k,obs}), \quad (3)$$

where $\hat{Y}^{k-1}$ is based on the maximum a posteriori (MAP) estimate of the traffic state at time step *k* – 1.

3.1.3 Factoring and Factor Graph Representation

Let $V=\{V_\alpha \mid \alpha \in V\}$ be a discrete valued random field with the probability mass function (pmf), $\pi(\mathbf{v})=\pi(i_1,\ldots,i_{|V|})$. The random field *V* is a Markov random field (MRF) if it satisfies the Markovian property

$$P(V_\alpha=i_1|V)=P(V_\alpha=i_1|V_{N_\alpha}), \quad (4)$$

for all $\alpha \in V$, where $\mathbf{N}_\alpha$ denotes the set of "neighbors" of α. These (conditional) independence assumptions between the variables V_α can be encoded in a graph $G=(V,\varepsilon)$ where V is indexed by the vertices (also called nodes) V such that $V=(V_s)_{s\in V}$ and edges (or arcs) $\varepsilon \in V \times V$. Note that the vertices coincide with the vehicles themselves; it is for this reason that the same notation is used in both cases. In this study, the edges ε connect the (speeds of) vehicles, rather than the lattice cells, as the random variables of the MRF model. By encoding the spatial dependencies in the speed field through edges ε, the condition in (4) implies that speed of any vehicle is independent of the traffic state given the local speed field.

The joint probability distribution over all the variables in the Markov model can be compactly represented by defining a set of cliques $\{\mathcal{C}\}$, which are subsets of vertices of $\mathcal{G}$ such that all vertices in each clique $\mathcal{C}$ are completely connected or mutually adjacent. A clique is said to be maximal if no other vertex in $\mathcal{G}$ can be added without violating the clique property. The joint distribution of the MRF can be expressed over the maximal cliques, as a product of factors as [(102)],

$$\pi(\mathbf{v})=\frac{1}{Z}\prod_{c\subset G}\psi_c, \quad (5)$$

where *Z* is the normalizing constant, $\mathbf{v}_c$ is the restriction of $\mathbf{v}$ to the vertices in the clique *c*, and $\{\psi_c\}_{c\subset G}$ is a set of "factors" for each maximal clique $c \subset G$. Each factor is a non-negative

function defined over a clique to represent the (unnormalized) probability distribution between the nodes in the clique. When the potentials are restricted to be strictly positive, the factors can be re-parametrized in the log space and expressed in terms of the Boltzmann distribution as $\psi_c = e^{-E_c(\mathbf{v}_c)}$, where $\{E_c(\mathbf{v}_c)\}_{c\subset \mathrm{G}}$ are properly defined potential functions over the cliques.

Consider the case where probe vehicles are equipped with sensors capable of measuring distances and speeds of other vehicles that are immediately adjacent (their immediate leaders and followers). In this case, the look-ahead potentials are encoded into *node factors*, $\{\psi_\alpha^k\}_{\alpha\in \mathrm{V}}$, and interaction potentials into *edge factors*, $\{\psi_{\alpha,\beta}^k\}_{(\alpha,\beta)\in\varepsilon}$. (When two vehicle indices appear in the subscript, the factor is to be implicitly understood as an edge factor.) Figure 3-1 presents a factor graph representation of a system with five vehicles, i.e., V = {1, …, 5} and interaction between adjacent vehicles. The vehicle speeds are presented by circular nodes in the graph. Factors are represented by square nodes in the graph, where the set $\{\psi_\alpha^k\}_{\alpha\in \mathrm{V}}$ are the factors pertaining to look-ahead dynamics, while $\{\psi_{\alpha,\beta}^k\}_{(\alpha,\beta)\in\varepsilon}$ are factors pertaining to vehicle interactions

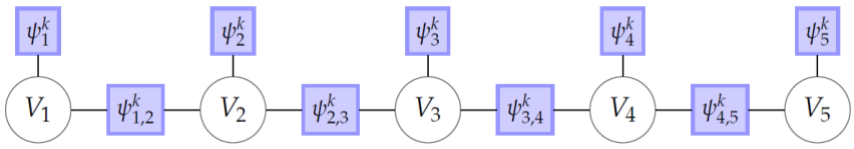

Figure 3-1 Example factor graph

The algorithm is a generalization of the variable elimination algorithm to execute multiple queries on the same tree-structured graph efficiently by guiding the order of operations. This is achieved by fixing any node as the root of the graph and determining the order in which the messages are propagated from the root to all its leaves by a depth first search algorithm. Messages are sent from all the leaf nodes to the root node during a single forward pass shown as red arrows in Figure 3-2. The figure also indicates the order in which the nodes are traversed when the node V_7 is the root node. By then sending messages from the root node to the leaf nodes during a single backward pass and storing all the intermediate messages, the marginals over any subset of variables can computed without recalculation for every inference. More details can be found in standard references on graphical models/machine learning [102, 103].

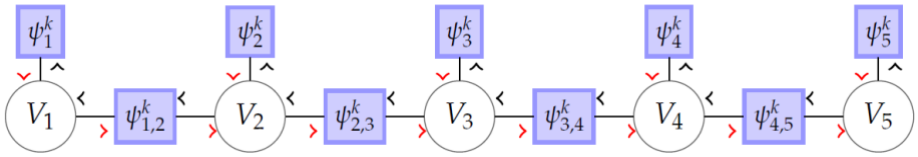

Figure 3-2 Illustration of forward (red arrows) and backward passes (black arrows) in the sum-product algorithm

When measurements are available for some of the vehicles, given by σk,obs, the inferences can be conditioned by clamping the corresponding variables to the observed states. As a consequence of conditional independence, when a node is observed, it breaks the chain structure into a forest of independent chains. For example, for the five vehicle system in Figure 3-1 and Figure 3-2, assuming $V_3 = 1$ is given (i.e., the speed of vehicle 3 is known/measured), the independent forest shown in Figure 3-3 is obtained.

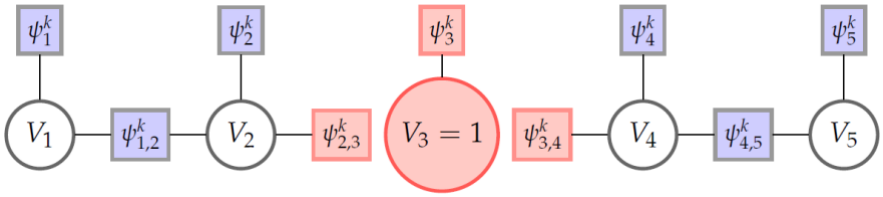

Figure 3-3 Decomposition of the factor graph into a forest of independent sub-graphs in the presence of measurements

3.1.4 Model Testing and Validation

Numerical Test: Shockwave

Consider a road of length N cells with $v_{max} = 3$ and assume an arrival density at the upstream end of $p_1 = 0.25$. At the upstream boundary, loop detectors provide information about the occupancy and speed of all upstream vehicles, as well as the entry times of new vehicles into the road. In order to validate the model (with out-of-sample data), an incident is simulated at the downstream boundary of the road section. The simulated traffic dynamics are illustrated in Figure 3-4(a), which represents ground truth and used for comparison with the traffic dynamics reconstructed by the CRF model. The interface between the free-flow (red) part of the figure and the congested (green and black) part of the figure represents the propagation of congestion from the source of the incident at the top of the figure into the upstream (against the direction of traffic). The trajectory of the interface represents a shockwave in the traffic stream. A subset of all the simulated vehicles are chosen randomly to represent a set of probe

vehicles. For this study, periodic noise-free updates of the vehicle position and speed (obtained from successive GPS coordinates) are assumed to be available from the probe vehicles at a (time) cadence of once every 1 seconds. Consequently, v_{max} = 3 cells and cell lengths of 7.5 meters correspond to a maximum speed of 81 km/hr. The CRF model is used to estimate the speed field sequentially in discrete time-steps, which correspond to the sampling interval of the probe vehicles. The estimated vehicle trajectories are shown in Figure 3-4(b), indicating that a probe penetration rate of 10% is sufficient to capture the backward propagation of a shockwave generated by the incident located downstream.

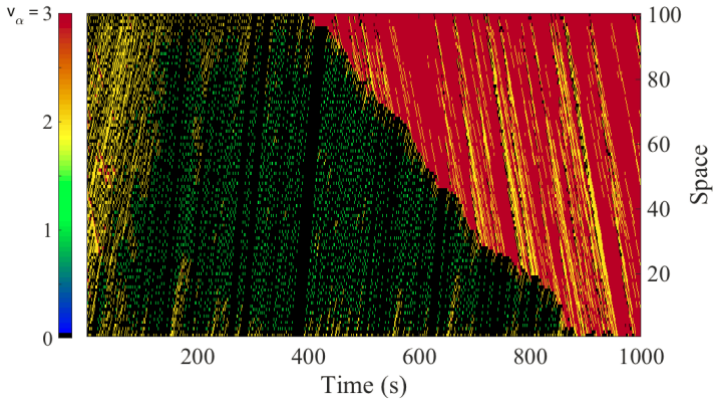

(a) Ground truth

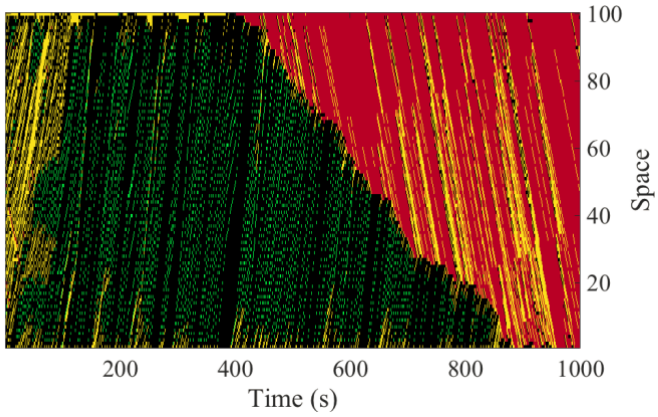

(b) Probe penetration=10%

Figure 3-4 Validation of CRF model

Learning Traffic Dynamics from Historical Data

In this experiment, "historical datasets" are simulated for a road section using a microscopic traffic simulation tool. The simulations are run for 1 hour periods (from 8 am to 9 am) with a 15 minute warm-up period for an arterial link that is 500m long. The vehicle trajectory data, collected from the simulation, is a sequence of spatial co-ordinates sampled every 1 second. This continuous trajectory data is discretized by dividing the roadway into a cell lattice (with cell

lengths 7.5m). The free-flow speed along the arterial link is 120 km/hr, and a fixed-time signal is located at the downstream end with a green time of 90s. In order to generate sufficient historical data, datasets are generated for different traffic conditions by varying the random seed as well as by considering different traffic flow conditions. The effect of increasing the probe penetration rate on the estimated traffic states is shown in Figure 3-5, which indicates that a penetration rate of 10% is not adequate for learning the traffic dynamics. The results also show that with a single set of historic data to learn from, in order to capture the ground truth conditions with sufficient accuracy, a probe penetration of 20% or more is needed. This is compared to the case where historical data are used to fit the parameters of the model in Figure 3-6. After ten learning phases, it can be observed from Figure 3-6 that even with a 10% probe penetration, vehicle trajectories can be reconstructed faithfully (comparable to using standard estimation techniques with a 30% probe penetration rate).

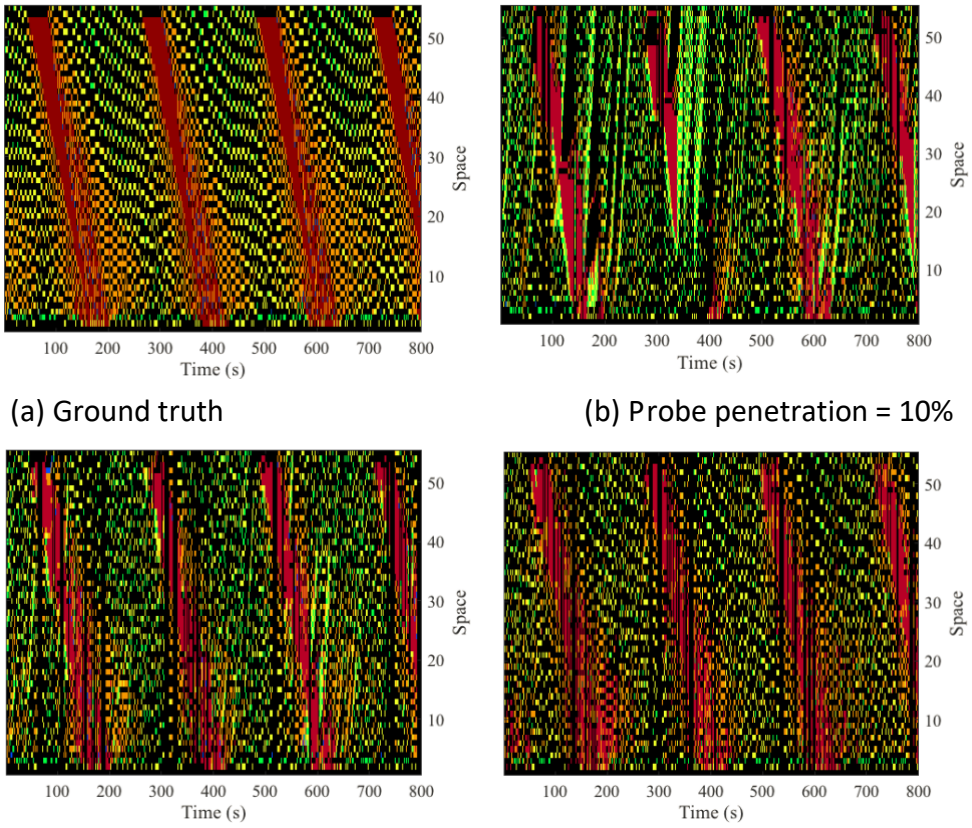

(a) Ground truth

(b) Probe penetration = 10%

(c) Probe penetration = 20%

(d) Probe penetration = 30%

Figure 3-5 Spatio-temporal velocity map. Black cells correspond to speeds i = 0, green to i = 1, yellow to i = 2, and red to i = vmax = 3

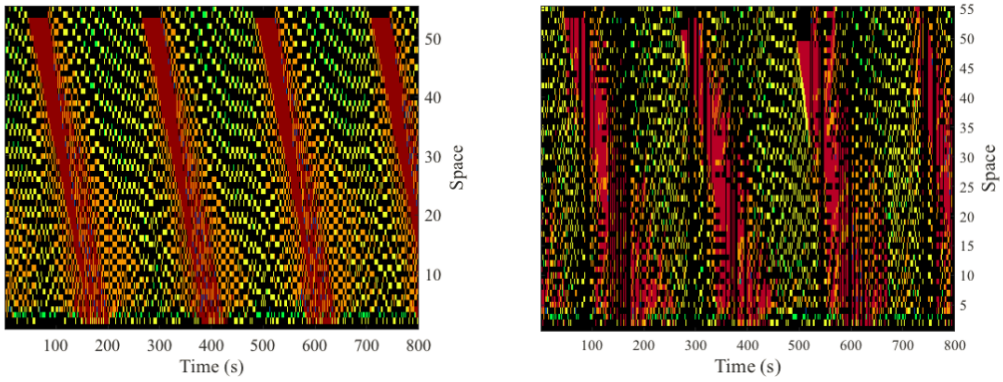

(a) Without historical data (b) With historical data

Figure 3-6 The effect of utilizing historic data, i.e., learning, on the estimated traffic dynamics

Probe Vehicle Distribution

Accuracy of the estimation problem not only depends on penetration rates of probe vehicles, but also on how the probes are distributed in the sample. The estimated traffic states are compared for two random distributions of probes, both representing a penetration rate of 5%. Figure 3-7 depicts the distribution of the randomly selected probes in the upper half of the figure with the estimated trajectories in the lower half for a signalized arterial. In this experiment, three signal cycles are simulated with simulation time horizon of length T = 900 seconds with a red-time of 100 seconds. The cycles start at time steps k = 100, 400, and 700. While this information can be easily inferred from a probe level of 5% as shown in Figure 3-7(a), when none of the sampled probes pass through the third signal cycle the estimation algorithm fails to capture the build-up and dissipation of queues in the time period from 700 to 900 seconds: as can be seen in Figure 3-7(b).

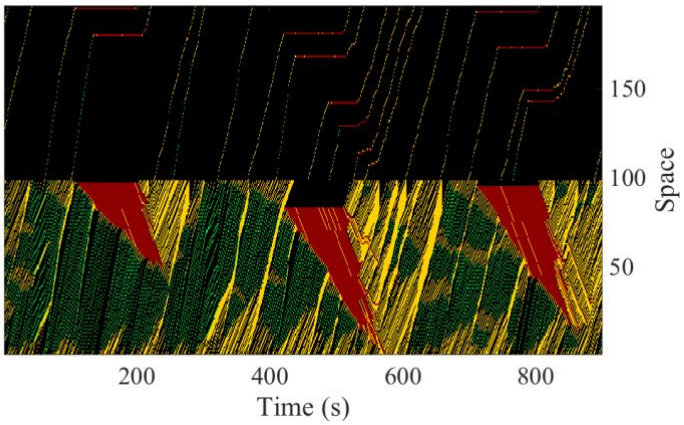

(a) Probe distribution 1

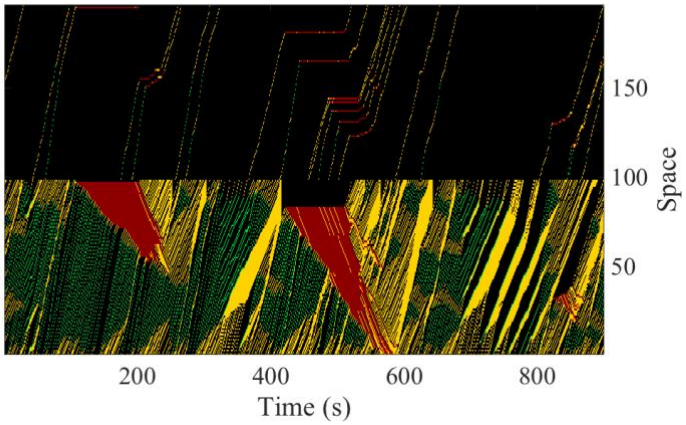

(b) Probe distribution 2

Figure 3-7 Different probe vehicle distributions

To study the effect of randomness in probe coverage (the distribution of the probes in the sample), a road segment with an on-ramp located at about 300 m downstream is considered. The free-flow speed was assumed to be 80 km/hr, while the traffic demand was gradually increased in 15 minute intervals from 1200 veh/hr to 2500 veh/hr to capture the build-up and dissipation of the on-ramp queues. The speed ranges correspond to the discrete speed states (the number of lattice cells crossed by a vehicle in a single time step).

The traffic state estimated for a time period of T = 15 minutes in congested conditions is depicted in Figure 3-8. When compared with the ground truth, the estimate produced with a probe penetration of 20% is sufficient to capture the shockwaves created by the on-ramp.

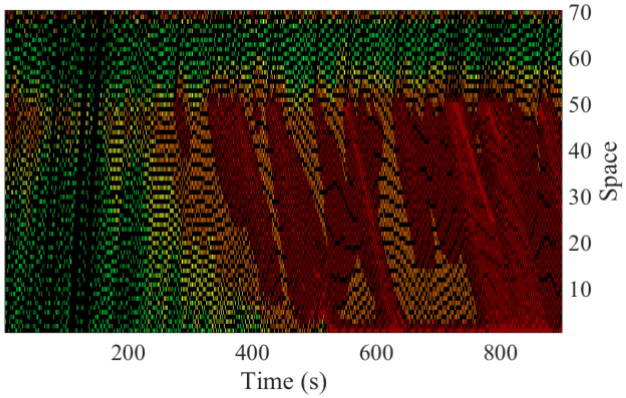

(a) Ground truth

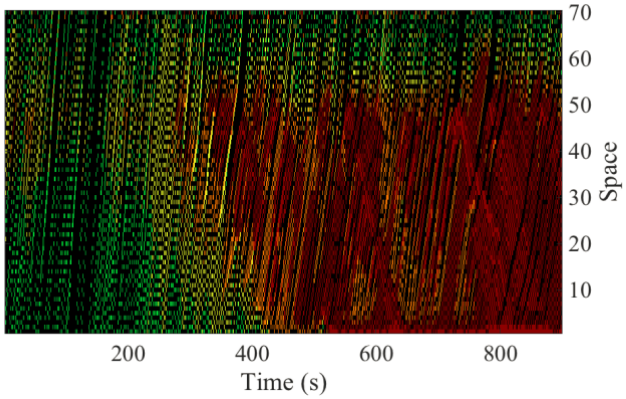

(b) Probe penetration = 20%

Figure 3-8 Time-space diagram (velocity)

It should be noted here that although no information regarding the entry times of the on-ramp vehicles was provided to our estimation algorithm, it can be inferred from the output in Figure 3-8(b). Similar estimation studies have indicated that probe levels of 2% can capture the shockwaves generated by lane-closure on a freeway [(104)]. However, in settings where the random arrivals of vehicles (e.g., on-ramp vehicles) significantly impact traffic flow, it is not surprising that a higher probe penetration rate is required for traffic state estimation in congested conditions. Moreover, as summarized in a study [(105)] on the microscopic estimation of freeway vehicles in a connected environment, for traffic signal control problems a minimum penetration rate of 20-30% is required, while for arterial performance measurement the penetration rate ranges from 10-50%.

The spatial distribution of the probe vehicles plays a significant role in the accuracy of estimated results, as observed earlier. To analyze the effect of the randomness introduced by the probe vehicle distribution, R = 100 simulations are run for each of the vehicle probe penetration rates, choosing a probe distribution randomly for each penetration rate. The following penetration rates are considered: 5%, 10%, 20%, and 30%. Figure 3-9 depicts the frequencies of the MAPEs for each of the penetration rates. The mean value of the MAPE for a probe penetration level of 5% is around 18%, but the high variability observed implies that travel time error can be even higher if the probe distribution is highly random. As the number of probe vehicles increases, this variability in the error decreases.

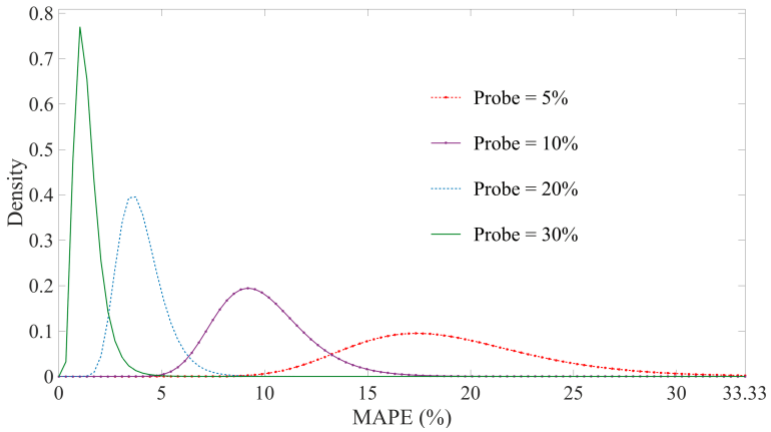

Figure 3-9 PDF of the Mean Absolute Percent Error in travel time at different probe levels

3.2 Traffic state estimation using stochastic Lagrangian dynamics

3.2.1 The traffic dynamics

Heterogeneous model

We assume a discrete system with N +1 vehicles numbered in descending order of position; that is vehicle n = 0 is the leader, n = 1 is the immediate follower, and so on. We assume a finite time horizon $T < \infty$ and that time is continuous (i.e., $T \in \mathrm{R}_+$). Let $x_n(t)$ and $v_n(t)$ denote the position and speed of vehicle n at time $t \in [0, T]$, respectively. We denote the spacing between vehicle n and their leader, $n - 1$, by

$$s_n(t) \equiv x_{n-1}(t) - x_n(t), \tag{6}$$

Heterogeneity in the driver population is represented by driver-specific speed-spacing relations. Without loss of generality, we adopt the Newell-Franklin (stationary) speed-spacing relation [59, 60]:

$$V_n(s) = v_{n,\mathrm{f}} - v_{n,\mathrm{f}} e^{\frac{-c_n}{v_{n,\mathrm{f}}}(s-d_n)}, \tag{7}$$

where the driver-specific parameters ($v_{n,\mathrm{f}}$, d_n, c_n) represent driver n's desired (free-flow) speed, minimum safety distance, and the constant cn is the inverse of the reaction time of driver n when their speed is restricted by the trajectory of their leader. In addition to the properties discussed in [60], this choice is inspired by the unique inverse function (Opposed, for instance, to Newell's simplified relation [61].), which can be used in data assimilation applications. Furthermore, the spacing dynamics can be simulated using the following recursion:

$$s_n(t+\Delta t) = s_n(t) + \Delta t \cdot \left(V_{n\text{-}1}(s_{n\text{-}1}(t)) - V_n(s_n(t))\right), \tag{8}$$

In settings with homogeneous drivers, in which $(v_{n,f}, d_n, c_n) = (v_{0,f}, d_0, c_0)$ for all $n \geq 1$, Δt is chosen so as to ensure no violations of the Courant-Friedrichs-Lewy (CFL) condition, i.e., $\Delta t \leq \Delta n / c_0$ and to mitigating numerical diffusion, one chooses the largest such time discretization: $\Delta t = \Delta n / c_0$.

An algorithm for simulating sample paths is given as below:

Require: N, Δn, T, $x_0(\cdot)$, $v_0(\cdot)$, $\{s_n(0)\}_{n=1}^{N}$, F_ϑ, $k \leftarrow 0$

1: **for** $n \leftarrow 1$ **to** $n \leq N$ **do**

2: $U_1, U_2, U_3 \sim$ Uniform$[0,1]^3$

3: $(v_{n,\mathrm{f}}, d_n, c_n) \leftarrow F_\theta^{-1}(U_1, U_2, U_3)$

4: **end for**

5: $\Delta t \leftarrow \min_{1 \leq n \leq N} \frac{\Delta n}{c_n}$

Iterate:

6: **while** $k \leq \lfloor T / \Delta t \rfloor$ **do**

7: $k \leftarrow k+1$

8: **for** $n \leftarrow 1$ **to** $n < N$ **do**

9: $v_n(k\Delta t) \leftarrow V_n(s_n(k\Delta t))$

10: $s_n(k\Delta t) \leftarrow s_n((k-1)\Delta t) + \Delta t\left(v_{n-1}((k-1)\Delta t) - v_n((k-1)\Delta t)\right)$

11: $x_n(k\Delta t) \leftarrow x_{n-1}(k\Delta t) - s_n(k\Delta t)$

12: **end for**

13: **end while**

Table 3-2 Algorithm for simulating a single sample path

Parametric uncertainty and stochastic dynamics

To introduce stochasticity, we let the parameters be random variables. We interpret this as uncertainty about the driver characteristics. To differentiate the stochastic case from the deterministic case, we write the (stochastic) parameters as functions of ω, where Ω ω is the random space. We assume the random triples (the parameters) constitute n independent draws from identically distributed joint distributions. That is, we define the parameter 189 vector $\vartheta(\omega) \equiv (v_f, d, c)(\omega)$ with joint distribution function F_ϑ and the parameter tuple for each driver n, θn = $(v_{n,f}, d_n, c_n)$, is drawn independently from this common distribution: $\vartheta_n \sim F_\vartheta$. The stochastic speed-spacing relation is given by:

$$V(s,\omega) = v_{\mathrm{f}}(\omega) - v_{\mathrm{f}}(\omega) e^{\frac{-c(\omega)}{v_{\mathrm{f}}(\omega)}(s-d(\omega))}, \tag{9}$$

3.2.2 Mean dynamics and variability

Mean speed-spacing relation. From the strong law of large numbers, we have that:

$$\frac{1}{M}\sum_{i=1}^{M} V^m(s,\omega) \to \bar{V}(s) \text{ almost surely,} \tag{10}$$

where $\bar{V}(s) \equiv \mathrm{E}V(s,\omega)$. Note that $\bar{V}(s) \neq \bar{v}_{\mathrm{f}} - \bar{v}_{\mathrm{f}} \exp(-(\bar{c}/\bar{v}_{\mathrm{f}})(s-\bar{d}))$, where $\bar{v}_{\mathrm{f}} \equiv \mathrm{E}v_{\mathrm{f}}(\omega)$, $\bar{c} = \mathrm{E}c(\omega)$, and $\bar{d} \equiv \mathrm{E}d(\omega)$. The right-hand side is a percentile speed-spacing relation (typically, a 0.5-percentile or equilibrium relation), while $\bar{V}(s)$ is a mean speed-spacing relation; see[58] for more details. An example comparison is shown in Figure 3-10.

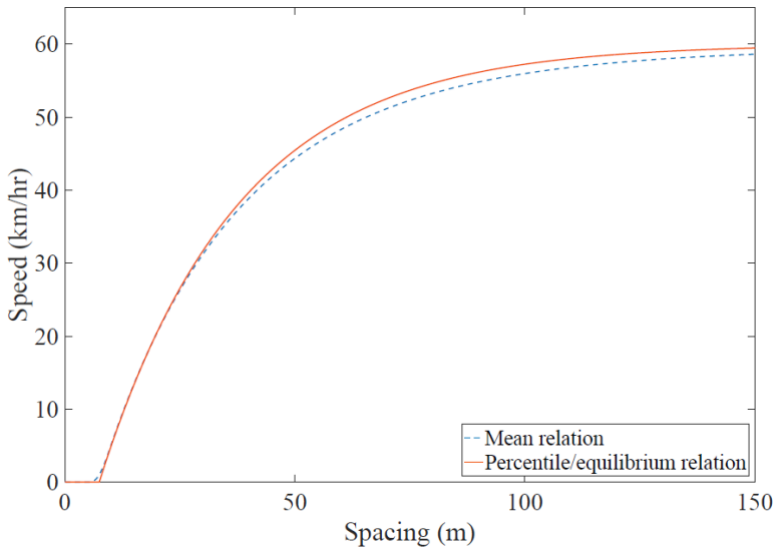

Figure 3-10 Mean relation, $\bar{V}(\cdot)$ vs. percentile relation.

Convergence result. The ensemble-average process converges to the mean dynamic is stated as follows:

$$\| s^M(\cdot,\omega) - \bar{s}(\cdot) \|_t \underset{M\to\infty}{\to} 0 \text{ for all } t \in [0,T]. \tag{11}$$

3.2.3 Numerical Testing

Consider a system with N = 200 vehicles (for example, made available by a fixed sensor in the system) and a time horizon of T = 1000 seconds. Assume a uniform spacing of 0.036 km at time t = 0, that is $s(0)$ = [0.036 · · · 0.036]⊺. The leaders speed trajectory is given by:

$$v_0(t) = \begin{cases} 0 \text{ km/hr} & \text{if } t \in (jT_r - T_r,\ jT_r] \text{ sec} \\ 60 \text{ km/hr} & \text{otherwise} \end{cases}, \tag{12}$$

where T_c = 120 seconds is the cycle length, T_r = 70 seconds is the red time, and j ∈ {1, …, 6}. The way we specify the leading vehicles trajectory is to create congestion such as vehicles waiting for the red signal at intersections. We assume in this example that $v_f(\omega)$, $d(\omega)$, and $c(\omega)$ are independent Beta random variables with supports $[v_f^{min}, v_f^{max}]$ = [40, 80] km/hr, $[d^{min}, d^{max}]$ = [5.88, 9.09] meters, and $[c^{min}, c^{max}]$ = [1100, 5100] veh/hr. We test the impact of increasing vehicle trajectory measurements on the uncertainty of traffic states in the system using algorithm in Table 3-3. Figure 3-11 depicts a sample path of the stochastic dynamics in terms of vehicle position trajectories and spacings.

Require: N, Δn, T, $x_0(\cdot)$, $v_0(\cdot)$, $\mathbf{z}(0)$, $\{\vartheta^j = (v^j_f, d^j, c^j)\}_{j=1}^{J}$ (historical data)

1: $\Delta t \leftarrow \frac{1}{J}\sum_{j=1}^{J}\frac{\Delta n}{c^j}$

2: $k \leftarrow 0$

Ensure:

3: **while** $k \le \lfloor T/\Delta t \rfloor$ **do**

4: $\hat{\mathbf{z}}((k+1)\Delta t-) \leftarrow \hat{\mathbf{z}}(k\Delta t)+\Delta t\mathbf{D}_{\mathbf{z}}\bar{\mathbf{V}}_{\mathbf{z}}(\hat{\mathbf{z}}(k\Delta t))$

5: $\hat{\mathbf{P}}((k+1)\Delta t-) \leftarrow \hat{\mathbf{P}}(k\Delta t)+\Delta t\left(\mathbf{D}_{\mathbf{z}}\bar{\mathbf{V}}_{\mathbf{z}}(\hat{\mathbf{z}}(k\Delta t))\hat{\mathbf{P}}(k\Delta t) + \hat{\mathbf{P}}^{\mathrm{T}}(k\Delta t)\mathbf{G}_{\mathbf{z}}^{\mathrm{T}}(\hat{z}(k\Delta t))\mathbf{D}_{\mathbf{z}}^{\mathrm{T}} + \Delta t\mathbf{D}_{\mathbf{z}}\boldsymbol{\Sigma}_{\mathbf{z}}(\hat{\mathbf{z}}(k\Delta t))\mathbf{D}_{\mathbf{z}}^{\mathrm{T}}\right)$

6: $\mathbf{r}((k+1)\Delta t) \leftarrow \mathbf{m}((k+1)\Delta t) - \mathbf{H}\hat{\mathbf{z}}((k+1)\Delta t-)$

7: $\mathbf{R}((k+1)\Delta t) \leftarrow \Delta t\mathbf{H}\hat{\mathbf{P}}((k+1)\Delta t-)\mathbf{H}^{\mathrm{T}}+\boldsymbol{\Omega}((k+1)\Delta t)$

8: $\mathbf{K}((k+1)\Delta t) \leftarrow \hat{\mathbf{P}}((k+1)\Delta t-)\mathbf{H}^{\mathrm{T}}\mathbf{R}^{-1}((k+1)\Delta t)$

9: $\hat{\mathbf{z}}((k+1)\Delta t) \leftarrow \hat{\mathbf{z}}((k+1)\Delta t-)+\mathbf{K}((k+1)\Delta t)\mathbf{r}((k+1)\Delta t)$

10: $\hat{\mathbf{P}}((k+1)\Delta t) \leftarrow \left(\mathbf{I}-\mathbf{K}((k+1)\Delta t)\mathbf{H}\right)\hat{\mathbf{P}}((k+1)\Delta t-)$

11: $k \leftarrow k+1$

12: **end while**

Table 3-3 Algorithm for Kalman-Bucy filter

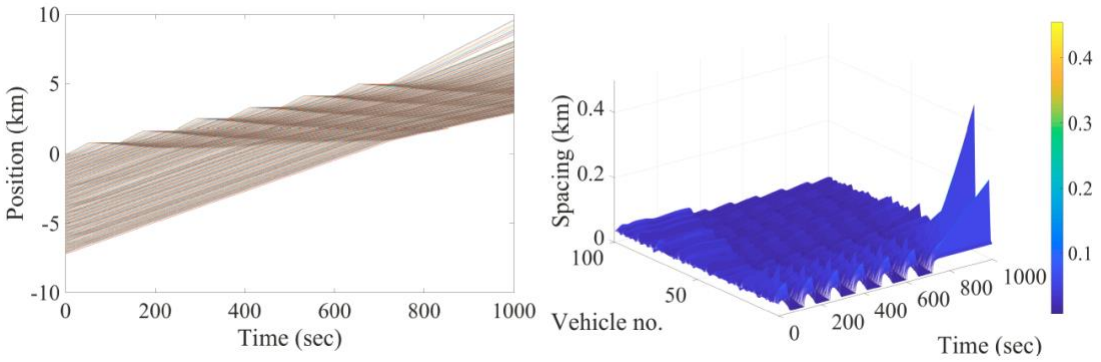

(a) (b)

Figure 3-11 Simulated sample paths; (a) position trajectories x(·), (b) spacings s(·).

To see the impact of data availability, we consider five cases of vehicle penetration rate: 5%, 10%, 20%, 30% and 50%. There is clear improvement in the estimate from low penetration rate (5%) to higher penetration rates (30%) as shown in Figure 3-12.

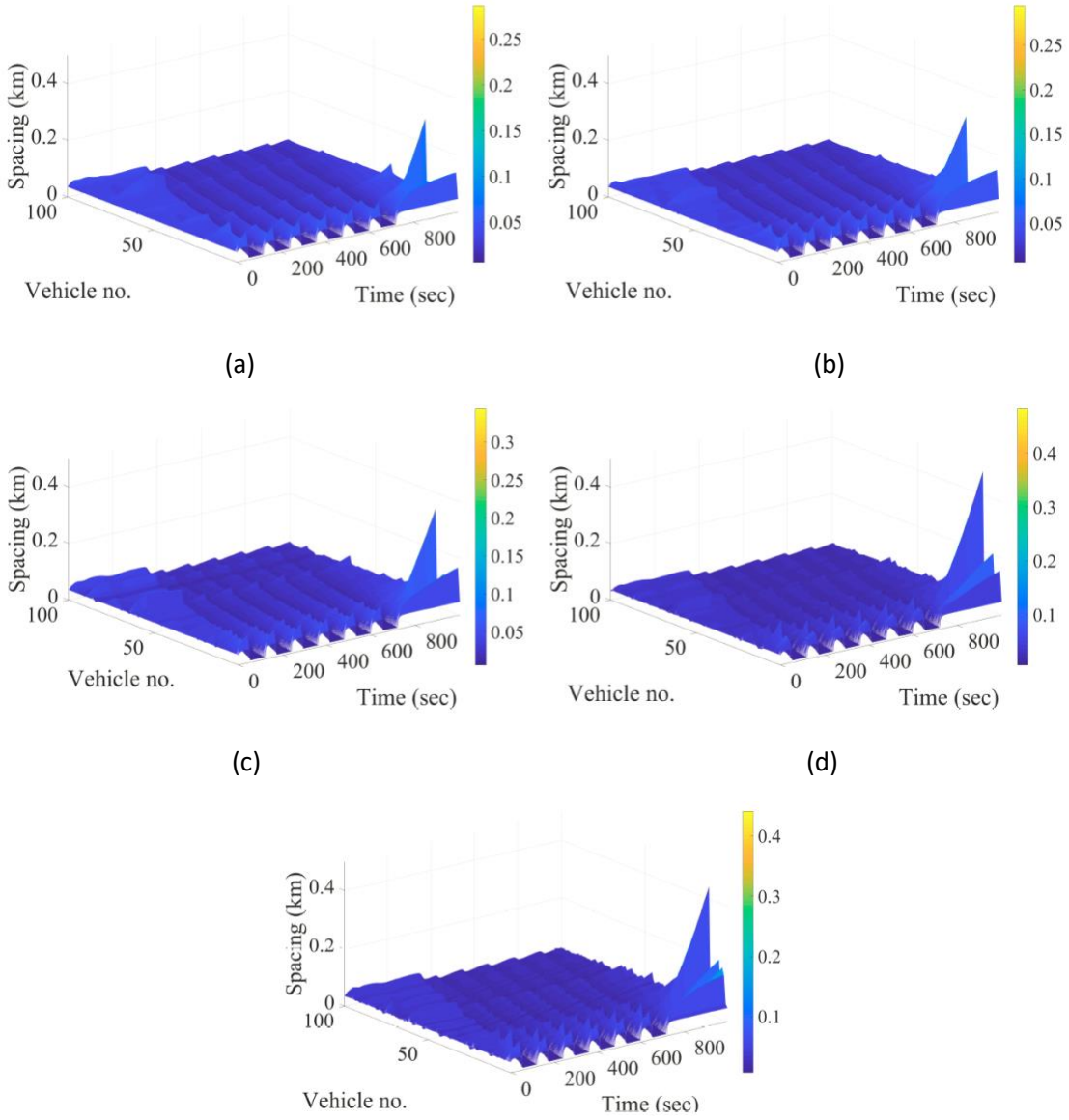

Figure 3-12 Estimated spacings with different penetration rates; (a) 5%, (b) 10%, (c) 20%, (d) 30%, and (e) 50%.

Table 3-4 illustrates the estimation performance for 200 vehicles in terms of Root Mean Square Error (RMSE) in spacing and Mean Absolute Percentage Error (MAPE) in spacing. The estimation performance is improved significantly when the penetration rate is higher than 20%.

Penetration rate	5%	10%	20%	30%	50%
RMSE (m)	11.5	11.4	11.4	7.3	6.2
MAPE (%)	17.6	17.5	17.1	14.4	12.2

Table 3-4 Estimation performance of spacings

Table 3-5 lists the RMSE and MAPE for the different penetration rates. It can be seen that increasing the penetration rate from 5% to 50% results in clear improvement of the estimation accuracy.

Figure 3-13 and Figure 3-14 depict the maximum queue sizes, along with 95% confidence intervals. Queue sizes are not direct state variables but computed based on the estimated spacing (mean and covariance) and corresponding speed.

Penetration rate	5%	10%	20%	30%	50%
RMSE (veh.)	1.15	0.91	0.82	0.71	0.41
MAPE (%)	2.54	2.05	1.56	1.15	0.79

Table 3-5 Queue size estimation performance

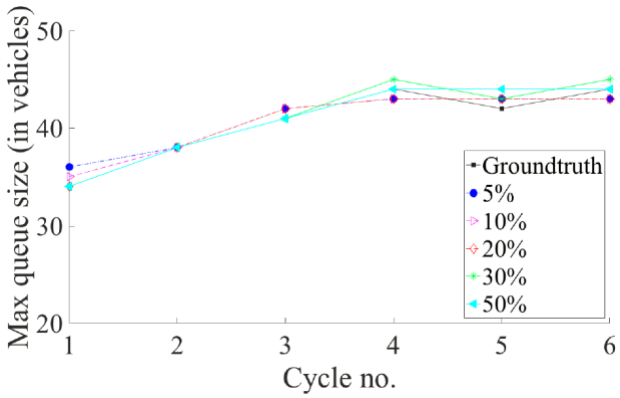

Figure 3-13 Maximum queue length by cycle.

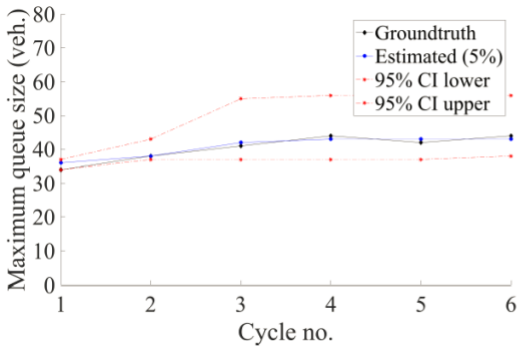

(a)

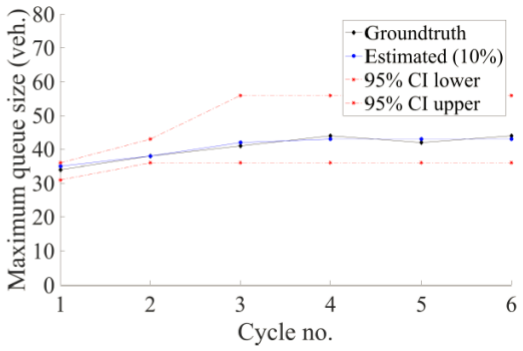

(b)

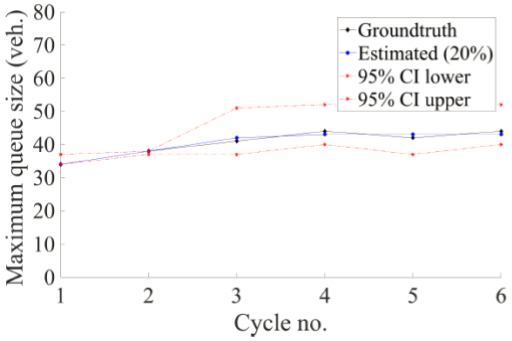

(c)

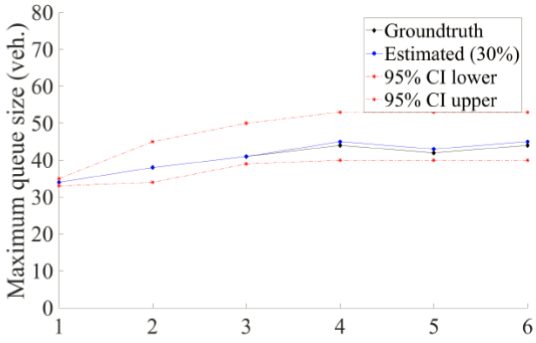

(d)

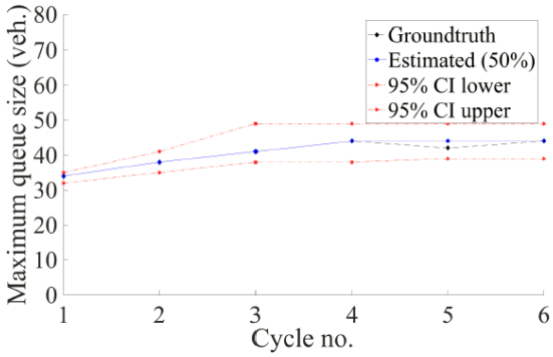

(e)

Figure 3-14 Maximum queue length along with 95% confidence intervals; (a) 5%, (b) 10%, (c) 20%, (d) 30%, and (e) 50%.

4 Position weighted backpressure intersection control

4.1 Notation

Consider an urban traffic network represented by the directed graph $\mathcal{G} = (\mathcal{N}, \mathcal{A})$, where $\mathcal{N}$ is a set of network nodes, representing intersections, and $\mathcal{A} \subset \mathcal{N} \times \mathcal{N}$ is a set of network arcs, representing road segments. Each element of $\mathcal{A}$ is in one-to-one correspondence with an ordered pair of elements in $\mathcal{N}$. For each node, $n \in \mathcal{N}$, $\prod_n$ and $\sum_n$ denote, respectively, the set of (predecessor) arcs terminating in n and the set of (successor) arcs emanating from n. We also use $\prod(a)$ to denote the set of predecessor arcs to arc $a \in \mathcal{A}$. That is, if n is the ingress node of arc a, then $\prod(a) = \prod_n$. Similarly, $\sum(a)$ is the set of successor arcs to arc a.

Fictitious source arcs are appended to the network to represent exogenous network arrivals. A new junction with indegree zero and outdegree one is created for each exogenous inflow and the new source arc connects this new node to the network boundary node; see Figure 4-1. When exogenous inflows occur at the interior of the network (i.e., at a junction with non-zero in-degree) representing, for example, a parking ramp/lot, the associated arc can be broken into two arcs with a new node placed at the position of the merge; see Figure 4-2. Source arcs will be assumed to have infinite jam densities (i.e., they serve as fictitious reservoirs), but the flow rates in and out of these arcs are assumed to be finite (i.e., finite capacities). They shall also be assumed to have zero physical length. Therefore, the traffic states associated with fictitious source arcs are point queues concentrated at the source node. We shall denote the set of (fictitious) source arcs by $\mathcal{A}^{\text{src}} \subset \mathcal{A}$.

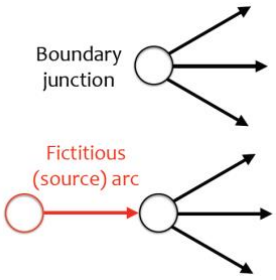

Figure 4-1 Fictitious boundary source arcs

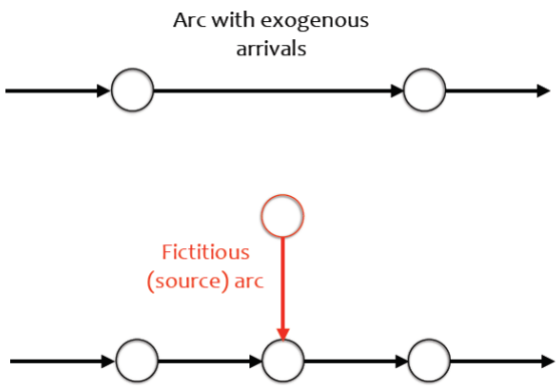

Figure 4-2 Fictitious interior source arcs

4.2 Dynamics

We denote the length of each arc $a \in \mathcal{A}$ by l_a. With slight notation abuse, the upstream-most position (the entrance position) for each arc a in the network is $x = 0$, while the downstream-most position (the arc exit position) is $x = l_a$ (that these coordinates pertain to arc a only should be understood implicitly). We consider a multi-commodity framework, where $\rho_a^b(x,t)$ denotes the traffic density at position x along arc a that is destined to outbound arc $b \in \sum(a)$ at time instant t. Similarly, $q_a^b(x,t)$ denotes the flow rate at x along a that is destined to b at time t. We have the following conservation equation: for each a in $\mathcal{A}$ and $b \in \sum(a)$

$$\frac{\partial \rho_a^b(x,t)}{\partial \mathrm{t}} = \frac{\partial q_a^b(x,t)}{\partial \mathrm{x}} \quad x \in [0, l_a], t \geq 0.$$

Let $p_{a,in}(t)$ and $p_{a,out}(t)$ denote the upstream and downstream control state at boundaries of arc a. The boundary flows are written as $q_a^b(0-,t) = q_{a,in}^b(p_{a,in}(t))$, and $q_a^b(l_a+,t) = q_{a,out}^b(p_{a,out}(t))$, where $q_{a,in}^b$ and $q_{a,out}^b$ are boundary flux functions, which depend on the (boundary) control variables and, implicitly, on the node dynamics (for instance, $q_{a,in}^b$ and $q_{a,out}^b$ cannot exceed local supplies and demands at the arc boundaries). We omit dependence on system state to minimize clutter in our notation.

We make no assumptions about the relationship between flux and density. The proposed approach is equally valid in first and second order contexts. The only assumptions we make are (i) flow conservation, (ii) probabilistic upper bounds on flux and density, and (iii) that arc parameters do not change along the length of the arc. The last assumption is easy to honor in a general network by splitting arcs with varying parameters into more than one arc.

4.3 Junction Control

For each node $n \in \mathcal{N}$, let $\mathcal{M}_n$ denote the set of allowed movements between inbound and outbound road segments. The set $\mathcal{M}_n$ consists of ordered pairs (a,b) such that $a \in \prod_n$ and $b \in$

$\sum_n$, i.e., $\mathcal{M}_n \subseteq \prod_n \times \sum_n$. The set of all network movements is denoted by $\mathcal{M} \equiv \mathcal{M}_1 \sqcup \cdots \sqcup \mathcal{M}_{|\mathcal{N}|}$. A signal phase consists of junction movements that do not conflict with one another. We denote by $\mathcal{P}_n \subseteq 2^{\mathcal{M}_n}$ the set of *allowable* phases and by $\mathcal{P} \subseteq \bigotimes_{n\in\mathcal{N}} \mathcal{P}_n$ the set of allowable network phasing schemes. Essentially, an allowable phase is one that does not allow crossing conflicts and only allows merging conflicts between a *protected* movement and a permitted movement. Example allowable phases are depicted in Figure 4-3. We denote by $q_{a,b}(p_{a,in}(t))$, or equivalently $q_{a,b}(p_{a,out}(t))$ the rate of flow that departs arc $a \in \prod(b)$ into arc b at time t. These are related to the commodity flows at the arc boundaries as follows:

$$q^b_{a,in}\left(p_{a,in}(t)\right) = \pi_{a,b}(t) \sum_{c\in\prod(a):(c,a)\in\mathcal{M}} q_{c,a}\left(p_{a,in}(t)\right)$$

and

$$q^b_{a,out}\left(p_{a,out}(t)\right) = q_{a,b}\left(p_{a,out}(t)\right),$$

where $\pi_{a,b}(t)$ is the percentage of flow into a at time t that is destined to adjacent arc $b \in \sum(a)$.

Under any network-wide phasing scheme, $p \in \mathcal{P}$, the traffic network can "support" arrival processes with certain rates. Beyond these arrival rates, queues will grow indefinitely. For each $p \in \mathcal{P}$, we say that the network can support an arrival rate vector $\boldsymbol{\lambda}(\mathrm{p}) = \left[\lambda_a(p) \cdots \lambda_{|A|}(p)\right]^{\mathrm{T}}$ if

$$\lim_{T\to\infty} \sum_{a\in A} \frac{1}{T} \int_0^T \left(\lambda_a(p) + q_{a,in}(p) - q_{a,out}(p)\right) \mathrm{d}t \le 0,$$

where with slight abuse of notation, $q_{a,in}(p)$ and $q_{a,out}(p)$ are the inflow and outflow rates obtained when the network phasing scheme p is active. This is interpreted as follows: the phasing scheme p is such that the total arc outflow exceeds the total arc inflow in the long run.

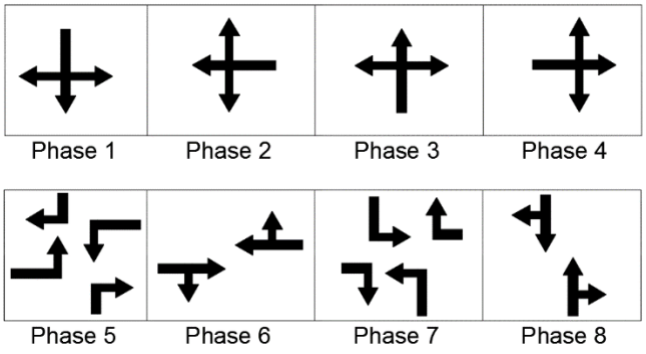

Figure 4-3 Example phases for a four-leg isolated intersection.

In accord with (7), each $p \in \mathcal{P}$ defines a set of admissible arrival rates; denote these (convex) polytopes by $\Omega(p)$. Taking the union of these sets, $\bigcup_{p\in\mathcal{P}}\Omega(p)$, we get the vectors of all possible arrival rates that the network can support under all $p \in \mathcal{P}$. This is formally defined next.

Definition 1 (Maximal throughput region). *The maximal throughput region (a.k.a., capacity region) of the network, denoted by* **Λ***, is the convex hull of all sets of admissible flows. That is,*

$$\mathbf{\Lambda} \equiv \mathrm{Conv}\left(\bigcup_{p\in\mathcal{P}} \Omega(p)\right).$$

Arrival rates that lie in **Λ** but not in $\bigcup_{p\in\mathcal{P}}\Omega(p)$are interpreted as arrival rates that can be supported by switching between phasing schemes that lie in the latter (i.e., *time-sharing*). A control policy that can support all possible arrival rates in **Λ** is referred to as a *throughput-maximal control policy*. We denote a control policy by a vector of network control states: at time t the network control state is denoted by $p(t) \equiv \left[\cdots\ p_{a,in}(t)\ p_{a,out}(t)\ \cdots\right]^{\mathrm{T}}$, a policy is an entire curve $p(\cdot)$.

4.4 Position-weighted back-pressure (PWBP)

For any intersection $n \in \mathcal{N}$, we assume that controllers are capable of assessing the (average) movement fluxes associated with any possible phase $p \in \mathcal{P}_n$. That is, for any $(a,b) \in \mathcal{M}_n$, $\mathbb{E}\left(q_{a,b}(p)|\boldsymbol{\rho}(t)\right) \equiv \mathbb{E}^{\boldsymbol{\rho}(t)} q_{a,b}(p)$ is known or can be estimated by the controller (locally). Drops in flux as a result of start-up lost times are captured by utilizing demand functions with diminishing flux at higher densities (see [101] and references therein). The stochasticity in the flows captures supply uncertainty. It can be modeled using parametric uncertainty [25, 58].

For each $n \in \mathcal{N}$ and each $(a,b) \in \mathcal{M}_n$, we define the *weight variable*

$$w_{a,b}(t) = c_{a,b}\int_0^{l_a}\left|\frac{x}{l_a}\right|\rho_a^b(x,t)\mathrm{d}x - \int_0^{l_b}\left|\frac{l_b-x}{l_b}\right|\sum_{\substack{c\in\sum(b):\\(b,c)\in\mathcal{M}}} c_{b,c}\pi_{b,c}(t)\rho_b^c(x,t)\mathrm{d}x$$

which depends on the (commodity) density curves along arcs a and b. To interpret this, first note that

$$\int_0^{l_a}\rho_a^b(x,t)\mathrm{d}x$$

is just the total traffic volume (queue size) along arc a that is destined to arc b. Then the first integral inside the square brackets in (9) can be interpreted as a weighted queue size, where traffic densities at the downstream end of arc a (at $x = l_a$) have the (maximal) weight of one, while traffic densities at the upstream end of a (at $x = 0$) have a weight of zero. In between, the weights increase linearly with x. Similarly, the second integral inside the square brackets in (9) can also be interpreted as a weighted queue size, but with the weights decreasing linearly with x. Hence, the weight associated with movement (a,b) decreases as the traffic densities at upstream end (ingress) of arc b increase and vice versa, and it increases when the traffic densities are concentrated at the downstream end of arc a and vice versa. The movement

constants $c_{a,b}$ in (9) allow for assigning higher weights to certain movements. For example, in our experiments, we use this to assign higher weights to left-turn movements: if (a, b) is a left-turning movement, $c_{a,b} \equiv (\frac{\#\text{thru}}{\#\text{left}})^2$, where #thru is the number of through lanes and #left is the number of left lanes. The phase that is active at node n at time t under PWBP control, denoted $p_{\text{PWBP}}(t)$, is given by

$$p_{\text{PWBP}}(t) \equiv \arg\max_{p \in \mathcal{P}_n} \sum_{(a,b) \in \mathcal{M}_n} w_{a,b}(t)\, \mathbb{E}^{\boldsymbol{\rho}(t)} q_{a,b}(p).$$

Since the number of possible phases at any intersection tend to be small (typically four-eight), (11) can be easily solved by direct enumeration. This allows for real-time distributed implementation of the proposed approach. It can also be demonstrated that PWBP control is *network stabilizing*.

In the proposed set-up, the density curves $\rho_a^b(\cdot, t)$ and the splits $\pi_{a,b}(t)$ are random quantities that are to be estimated or measured. In a fully automated system, these quantities may degenerate. That is, it is easy to imagine that they can be measured with high accuracy and become deterministic quantities. In present day settings, these quantities need to be estimated. The setting envisaged in this paper is one with mixed automated/connected and traditional vehicles. Connected vehicles announce their turning desires upon entering arc a and may serve as probes to allow the controller to estimate traffic conditions along the arc and the split variables. In such settings, the proposed control techniques need to be coupled with traffic state estimation tools; we refer to [25] and references therein for examples of traffic state estimation in urban traffic settings.

5 Experiments

5.1 Experiments for Lagrangian traffic estimation model

5.1.1 Microscopic traffic simulation experiments

Data preparation

The test area we selected is Plymouth Road, which is an urban arterial road in the city of Ann Arbor, Michigan. In order to obtain 'ground truth data', we utilize a calibrated microscopic traffic simulation model of the test road. Figure 5-1 provides an illustration of the test road (1km in length) with two intersections (Huron Pkwy - Plymouth Rd and Nixon Rd - Plymouth Rd). We derive the trajectory data (positions and speeds) of through-going vehicles traveling westbound along Plymouth Road over a time period of 600 seconds (see Figure 5-2). The parameters $v_f(\omega)$, $d(\omega)$, and $c(\omega)$ are independent Beta random variables with supports [v_{min} = [48, 58] km/hr, [d^{min}, d^{max}] = [5.8, 7.3] meters, and [c^{min}, c^{max}] = [1795, 3767] veh/hr estimated from the simulated ground truth trajectory data. We assume the first vehicle trajectory in the system and the initial condition (spacing of vehicles at time t = 0) are known as well.

Figure 5-1 The test road in Ann Arbor, Michigan.

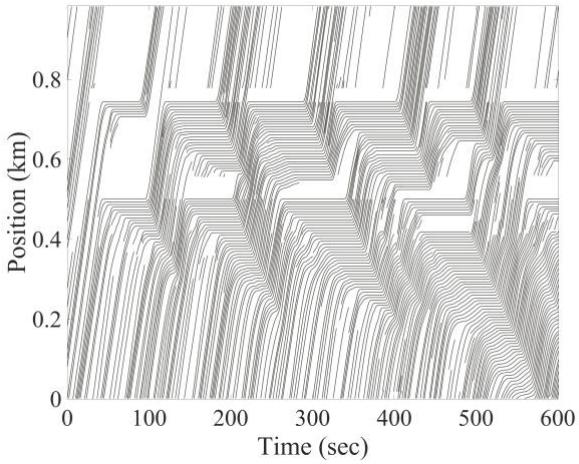

Figure 5-2 Ground truth from calibrated microscopic simulation model: position trajectories

To see the impact of data availability on the uncertainty of traffic state estimation, we consider five cases of penetration rate: 5%, 10%, 20%, and 30%and 50%. Figure 5-3 – Figure 5-5 illustrate the position trajectories available (the measurements) for the different penetration rates used in our experiments.

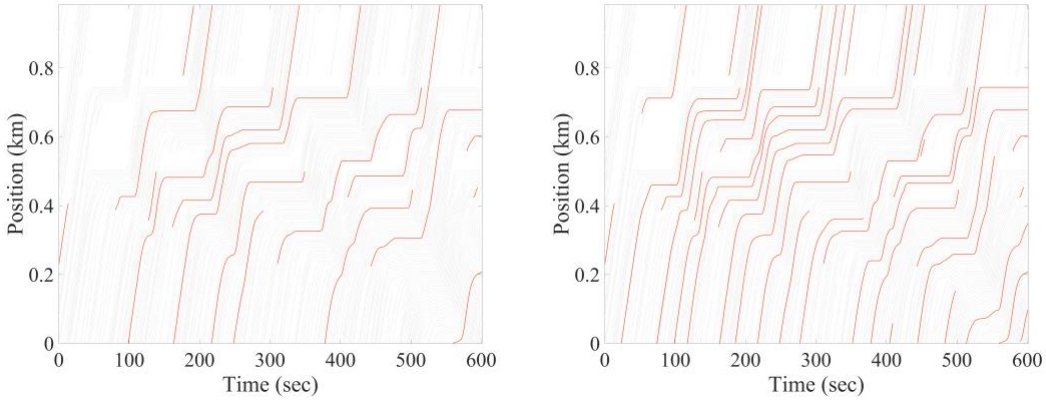

(a) (b)

Figure 5-3 Measured trajectories (bold) against the ground truth trajectories for penetration rates (a) 5% and (b) 10%.

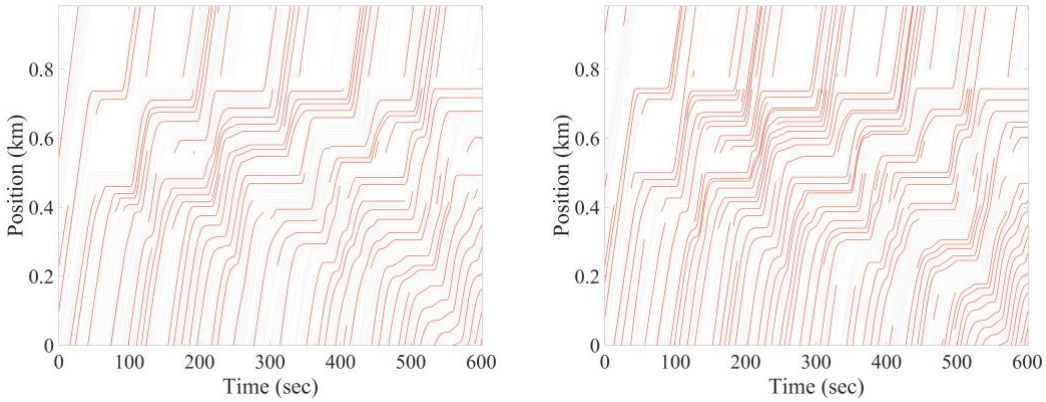

(a) (b)

Figure 5-4 Measured trajectories (bold) against the ground truth trajectories for penetration rates (a) 20% and (b) 30%.

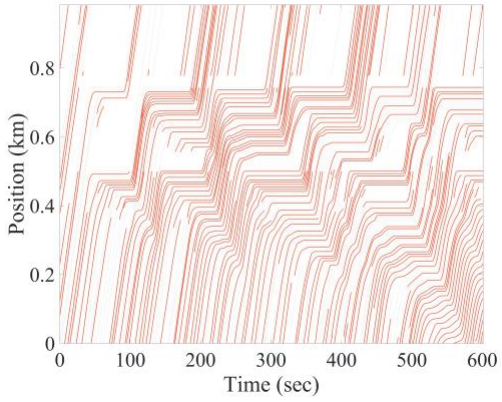

Figure 5-5 Measured trajectories (bold) against the ground truth trajectories for penetration rate 50%.

Estimation results

With estimated parameters of the model and given the first vehicle trajectory information (boundary condition) and the initial condition, the traffic state dynamics (spacing and positions) can be fully characterized. We apply the Kalman-Bucy filter given in Table 3-3. Figure 5-6 depicts the ground truth dynamics in terms of traffic densities and speed fields. Figure 5-7 and Figure 5-8 depict the estimated density and speed dynamics. There is clear improvement of estimation accuracy when the penetration rate increases from 5% to 50%. The congestion (shockwave) and queue dynamics can be well captured when the penetration rate increases to 20%. As a summary of the estimation accuracy, Figure 5-9 plots the RMSEs in speed for the varying penetration rates.

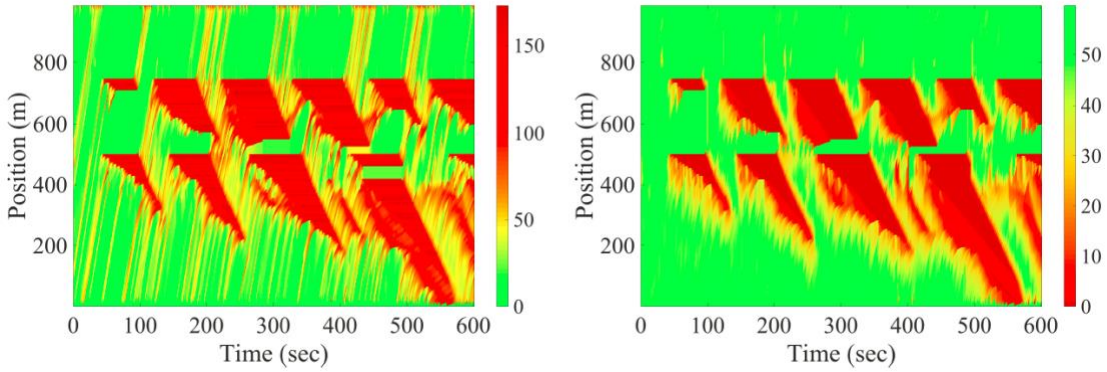

(a) (b)

Figure 5-6 Ground truth from calibrated microscopic simulation model: (a) density dynamics (in veh/km), (b) speed dynamics (in km/hr)

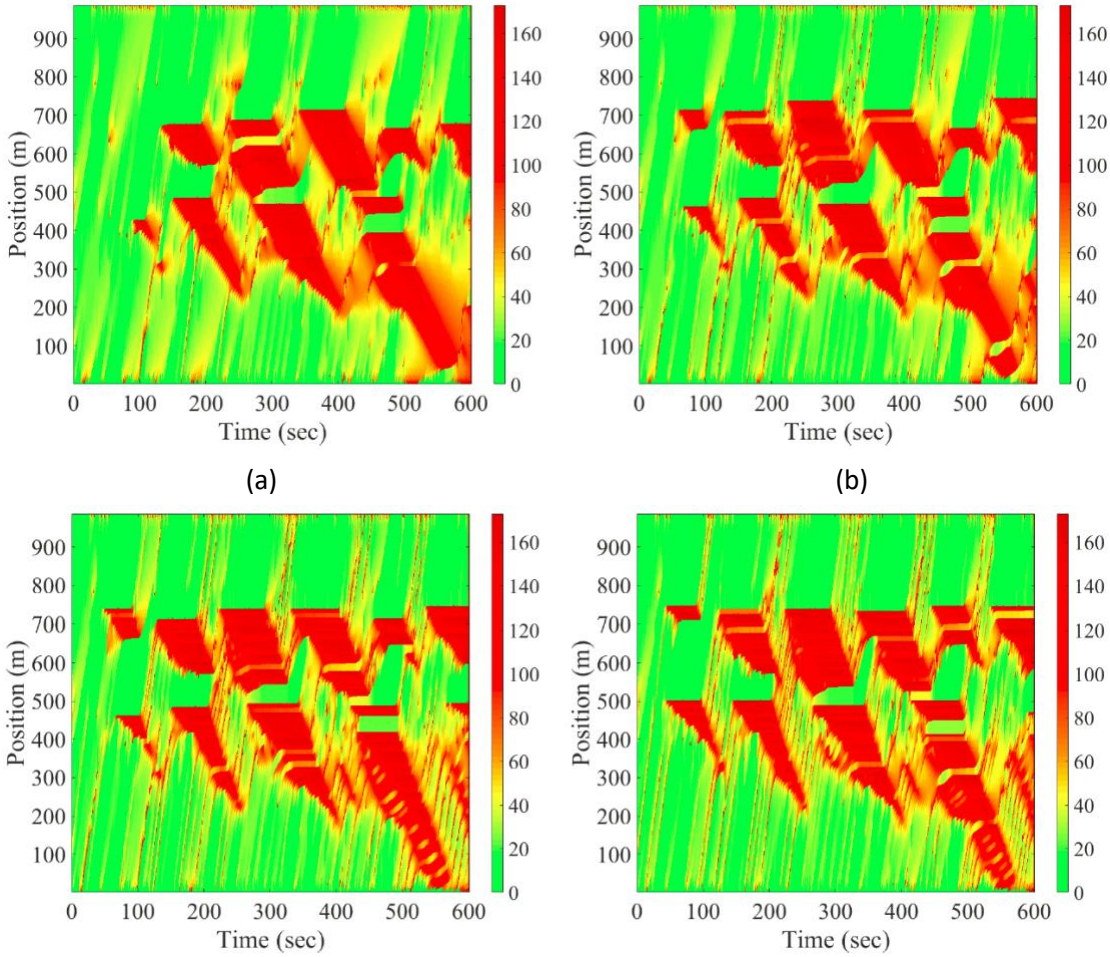

(a) (b)

(c) (d)

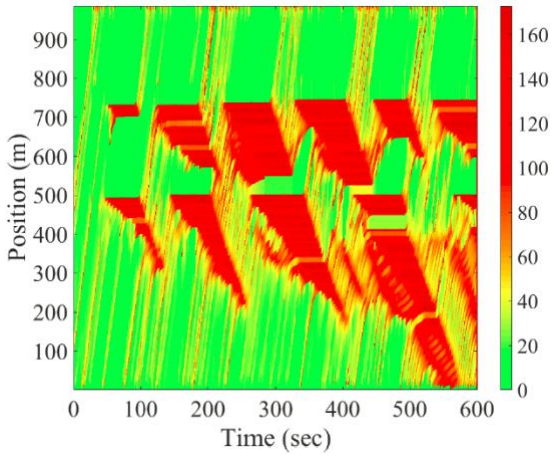

(e)

Figure 5-7 Estimated density fields (in veh/km) with different penetration rates: (a) 5%, (b) 10%, (c) 20%, (d) 30% and (e) 50%

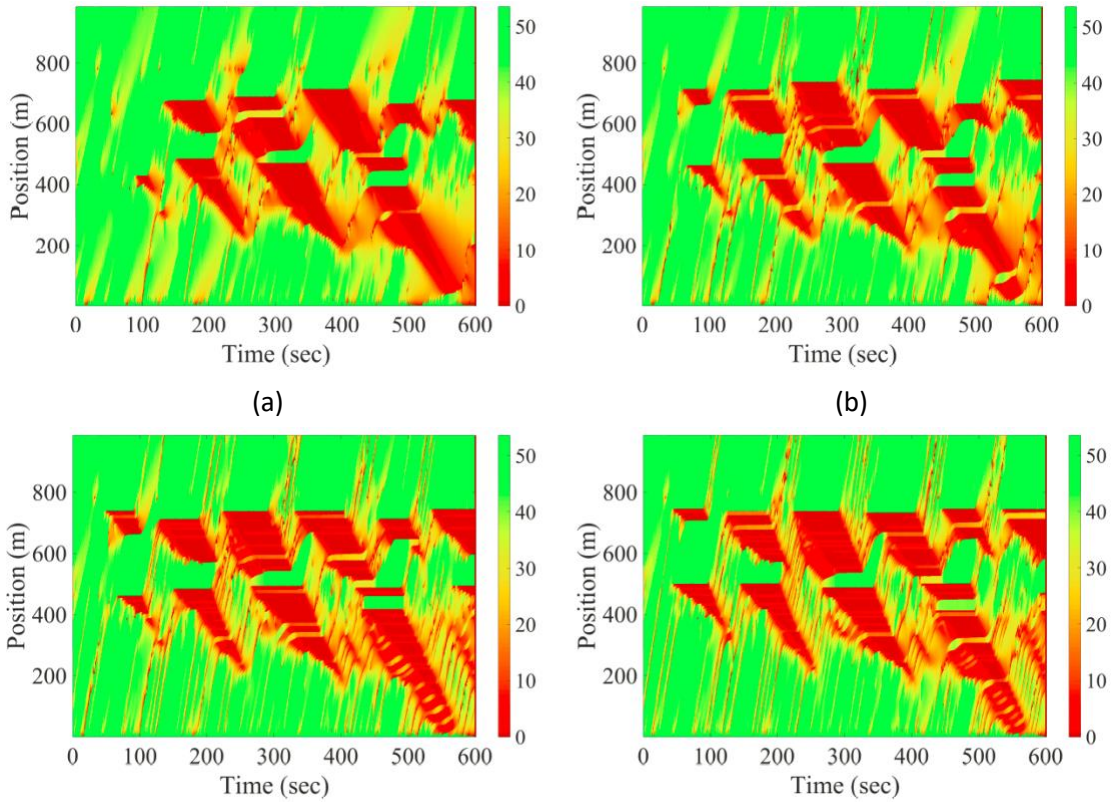

(a)

(b)

(c)

(d)

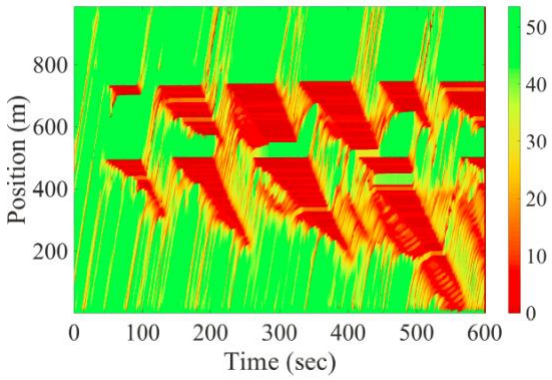

(e)

Figure 5-8 Estimated speed fields (in km/hr) with different penetration rates: (a) 5%, (b) 10%, (c) 20%, (d) 30% and (e) 50%

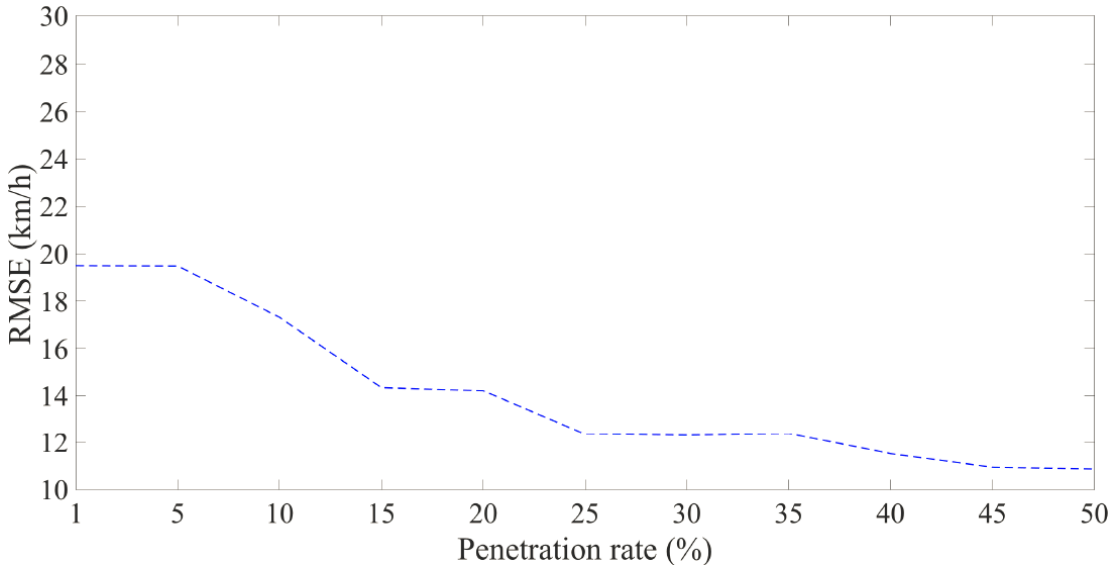

Figure 5-9 RMSE in speed estimates vs. probe penetration rate

5.1.2 NGSIM data experiments

Data preparation

In order to test the performance of the proposed model and estimation approach with field data, we use the NGSIM data collected on eastbound I-80 in the San Francisco Bay area in Emeryville, CA. The study area is approximately 500 meters in length and we selected the vehicle trajectory data on the farthest left lane with time period of 15min between 4:00PM and 4:15PM on April 13, 2005 (see Figure 5-10). Figure 5-11 - Figure 5-14 depict the sampled vehicle trajectory data for the four penetration rates.

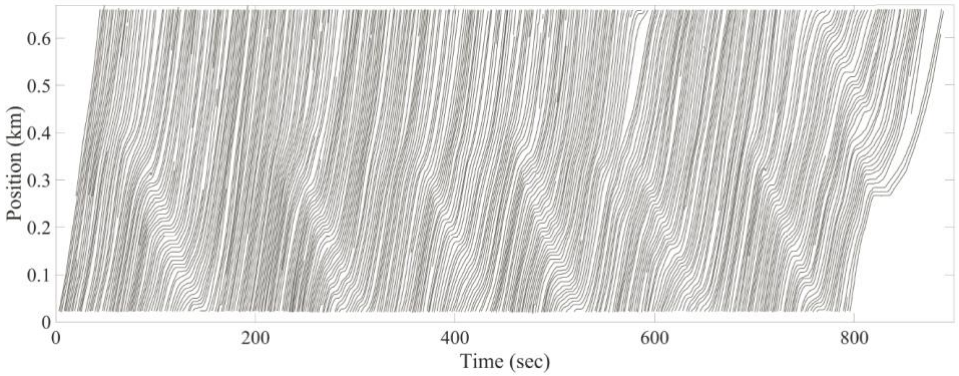

Figure 5-10 Ground truth vehicle trajectories along I-80

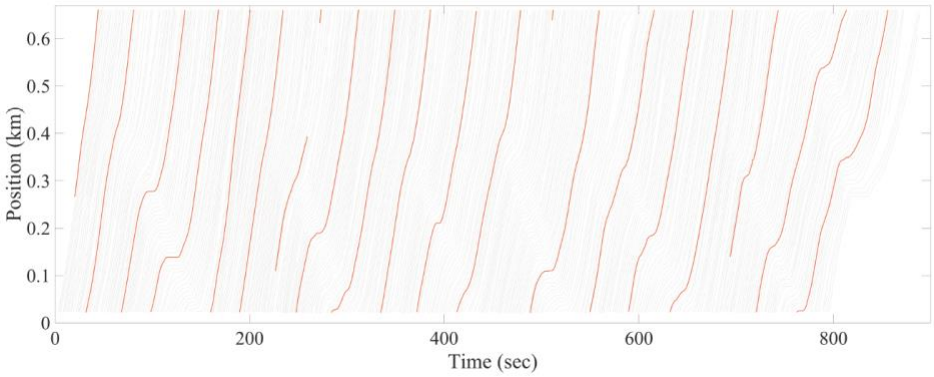

Figure 5-11 Sampled vehicle trajectories data for 5% penetration rate

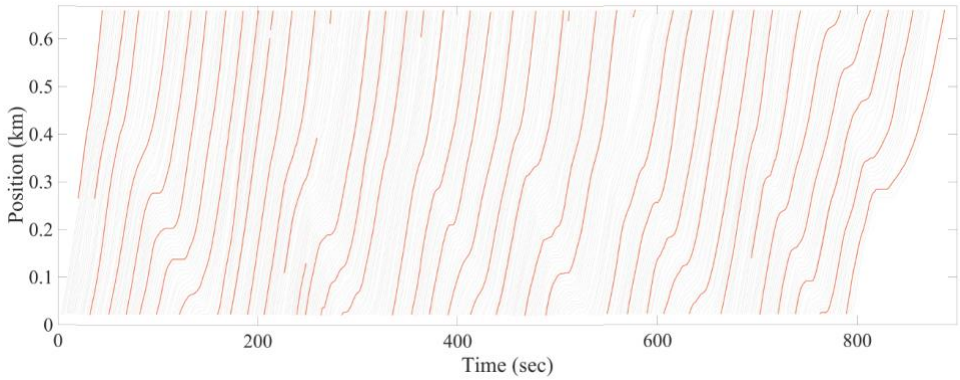

Figure 5-12 Sampled vehicle trajectories data for 10% penetration rate

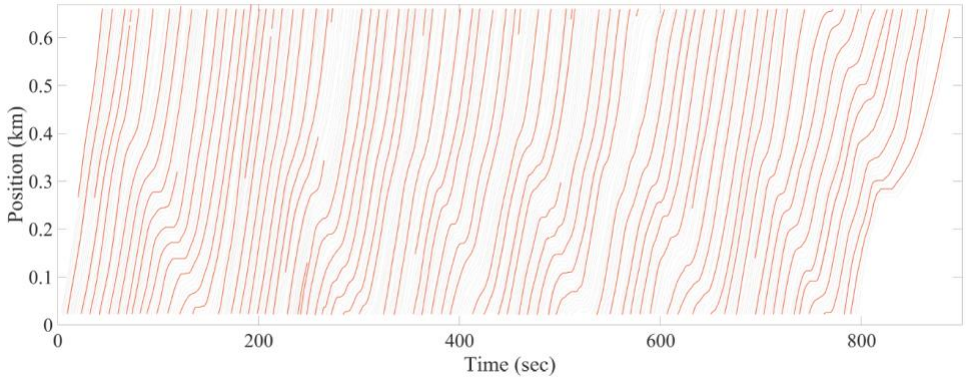

Figure 5-13 Sampled vehicle trajectories data for 20% penetration rate

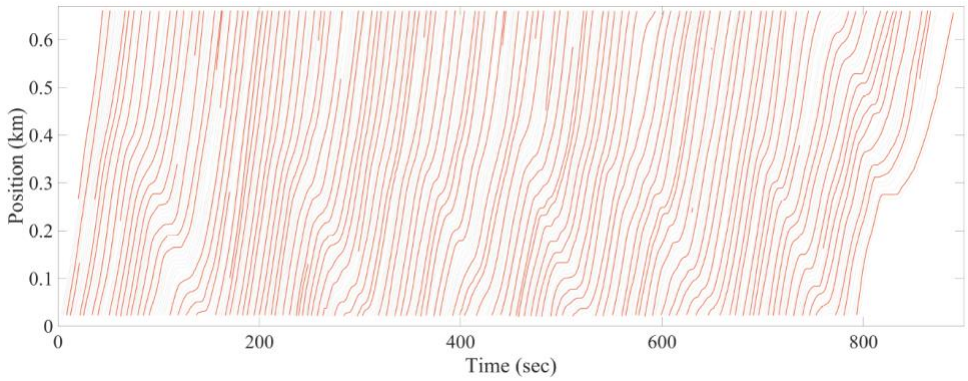

Figure 5-14 Sampled vehicle trajectories data for 30% penetration rate

The parameters $v_f(\omega)$, $d(\omega)$, and $c(\omega)$ are independent Beta distributed random variables with supports $[v_f^{min}, v_f^{max}] = [95, 105]$ km/hr, $[d^{min}, d^{max}] = [5.9, 7.7]$ meters, and $[c^{min}, c^{max}] = [2340, 3672]$ veh/hr. These were fitted using ground truth trajectory data.

Estimation results

We applied the proposed data assimilation approach to the second type of measurements, where we assume that spacing measurements are available, e.g., connected vehicles with their surrounding information available (both their leaders and followers) and spacings between the current vehicle and its immediate leader and follower can be measured (5 measurements). Figure 5-15 depicts the ground truth density and speed fields. To see the performance of the new measurement equation and the impact of data availability on the uncertainty of traffic state estimation, we consider four penetration rates: 5%, 10%, 20% and 30%.

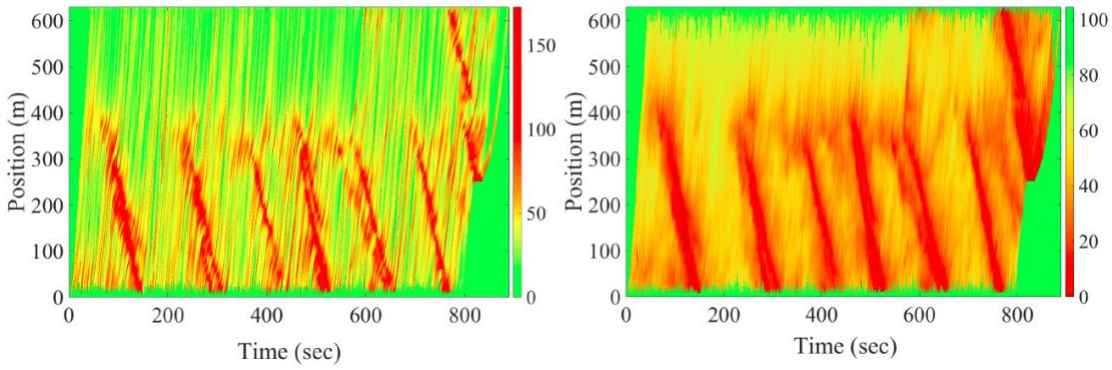

(a) (b)

Figure 5-15 Ground truth from NGSIM data: (a) densities (veh/km), (b) speeds (km/hr)

Figure 5-16 depicts the estimated density and speed dynamics. When the penetration rate increases from 5% to 10%, there is a clear improvement of density estimation accuracy. The congestion shockwave can be well captured when the penetration rate increases to 10%. Figure 5-17 depicts the estimated speed dynamics. When the penetration rate increases to 20%, the proposed approach is able to provide good estimation results in terms of congestion dynamics.

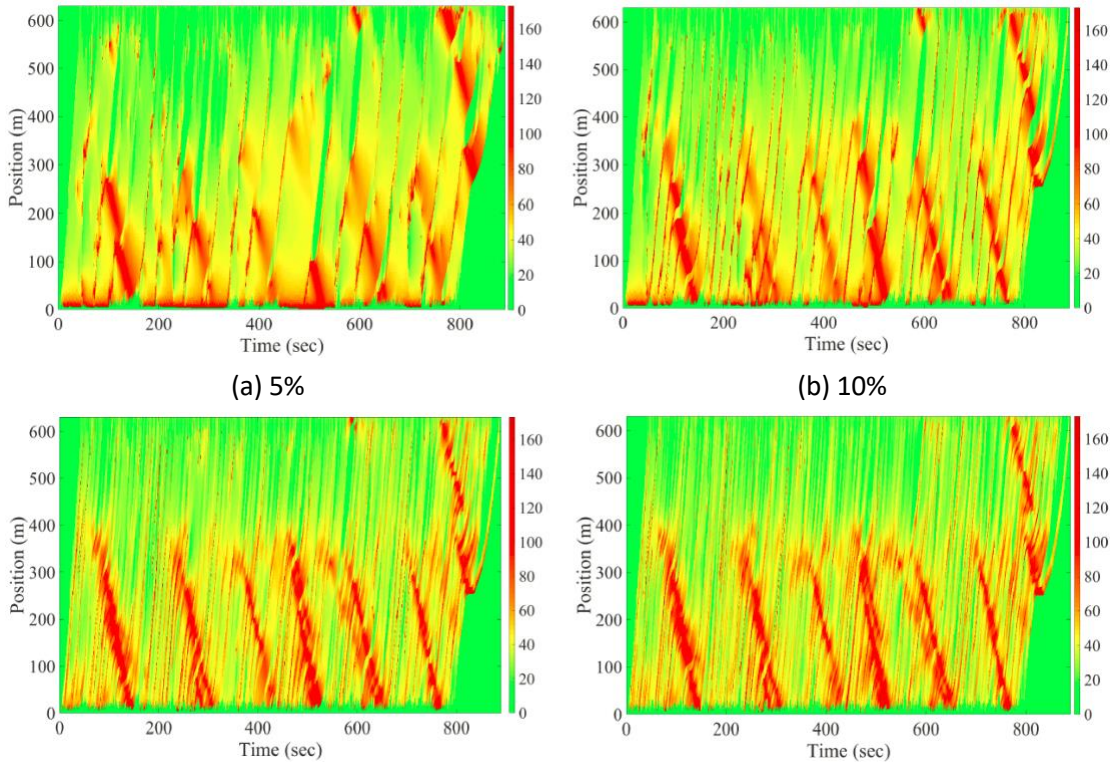

(a) 5% (b) 10%

(c) 20% (d) 30%

Figure 5-16 Estimated densities (veh/km) at different penetration rates

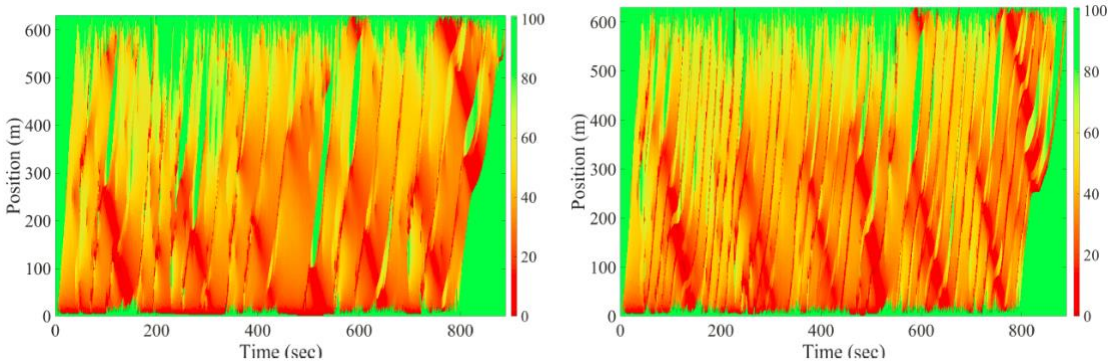

(a) 5% (b) 10%

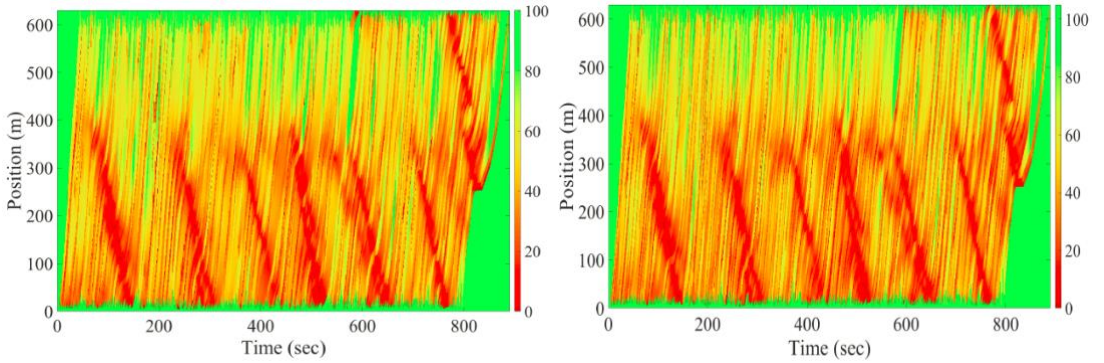

(c) 20% (d) 30%

Figure 5-17 Estimated speeds (km/hr) at different penetration rates

As a summary of the estimation accuracy, Figure 5-18 plots the RMSEs in speed for the varying penetration rates. The magnitudes of the RMSEs are comparable to most of the results in the literature, with the notable difference that our comparisons involve estimates of microscopic data.

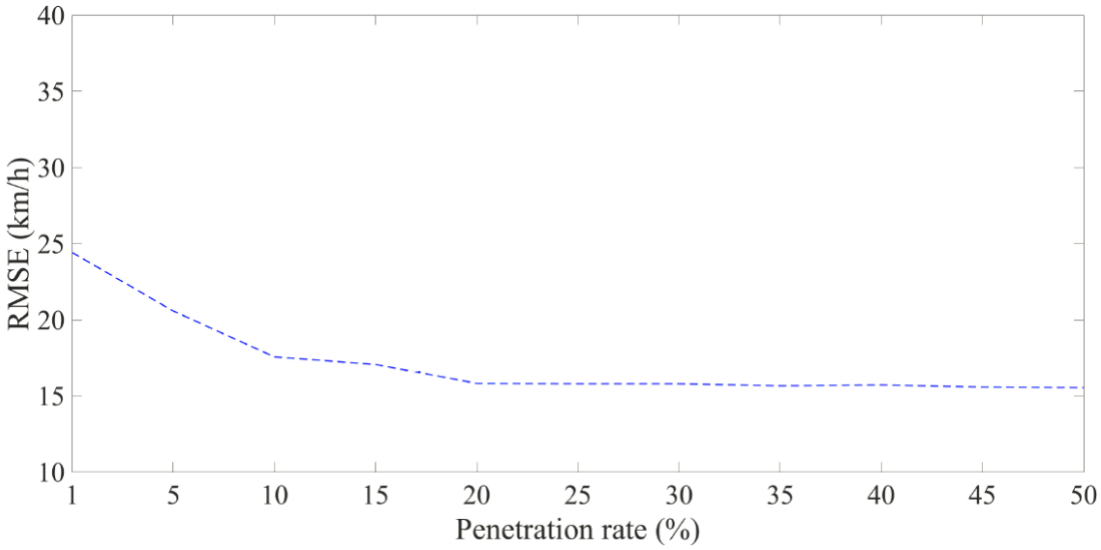

Figure 5-18 RMSE in speed estimates vs. probe penetration rate

5.2 Experiments for PWBP

5.2.1 Network description

We utilize a microscopic traffic simulation network of a part of the city of Abu Dhabi in the United Arab Emirates (UAE) consisting of eleven signalized intersections but also containing unsignalized intermediate junctions. The network layout is shown in Figure 5-19. We compare PWBP control with three other control policies: fixed time, standard BP control, and CABP control. The fixed timing plans are optimized and include optimal offsets (i.e., signal coordination). BP, CABP, and PWBP are all implemented using a software interface. To simplify the experiments, we utilize a uniform demand at the boundaries, which we vary to gauge the capacity region of the network. Using a uniform (average) demand level allows us to use a single number (namely the demand) as a way to gauge the capacity region.

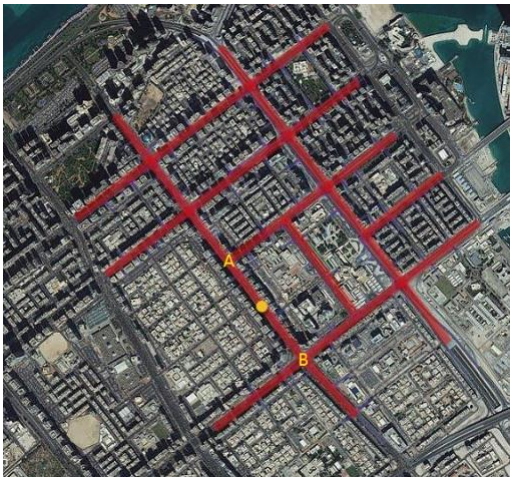

Figure 5-19 Simulation network in Abu Dhabi.

5.2.2 Average network delay and network capacity region

Figure 5-20 shows the total network delay under different demand scenarios (ranging from 500 to 1800 veh/h on average) for BP, CABP, and PWBP using two types of phasing schemes: one with four phases ("4-phase" scheme) and a scheme with eight phases ("8-phase scheme"). The 4-phase scheme includes phases 1-4 in Figure 4-3, while the 8-phase scheme is all eight phases in Figure 4-3. We observe that 40 s/veh is a threshold delay, beyond which the delay increases dramatically. We can hence treat 40 s/veh as indicative of reaching the boundary of the capacity region. From Figure 5-20, with the 8-phase scheme, we see that delays begin to increase rapidly at higher average demand levels for the PWBP: 1620 veh/h for the 8-phase scheme vs. 1580 veh/h for the 4-phase scheme. However, this is not the case for BP and CABP control, since they do not distinguish left-turning and through queues, which results in blocking

at the points where roads widen (left-turn lane addition). This indicates that BP and CABP have a wider capacity region using a 4-phase scheme compared to the 8-phase scheme. All subsequent experiments use an 8-phase scheme with PWBP and 4-phase schemes with BP and CABP. The demands at which delays begin to increase quickly for fixed signal timing, BP, CABP, and PWBP are 1225, 1555, 1570, and 1620 veh/h, respectively. Figure 5-21 shows a comparison of network delays for the four control policies under varying demands.

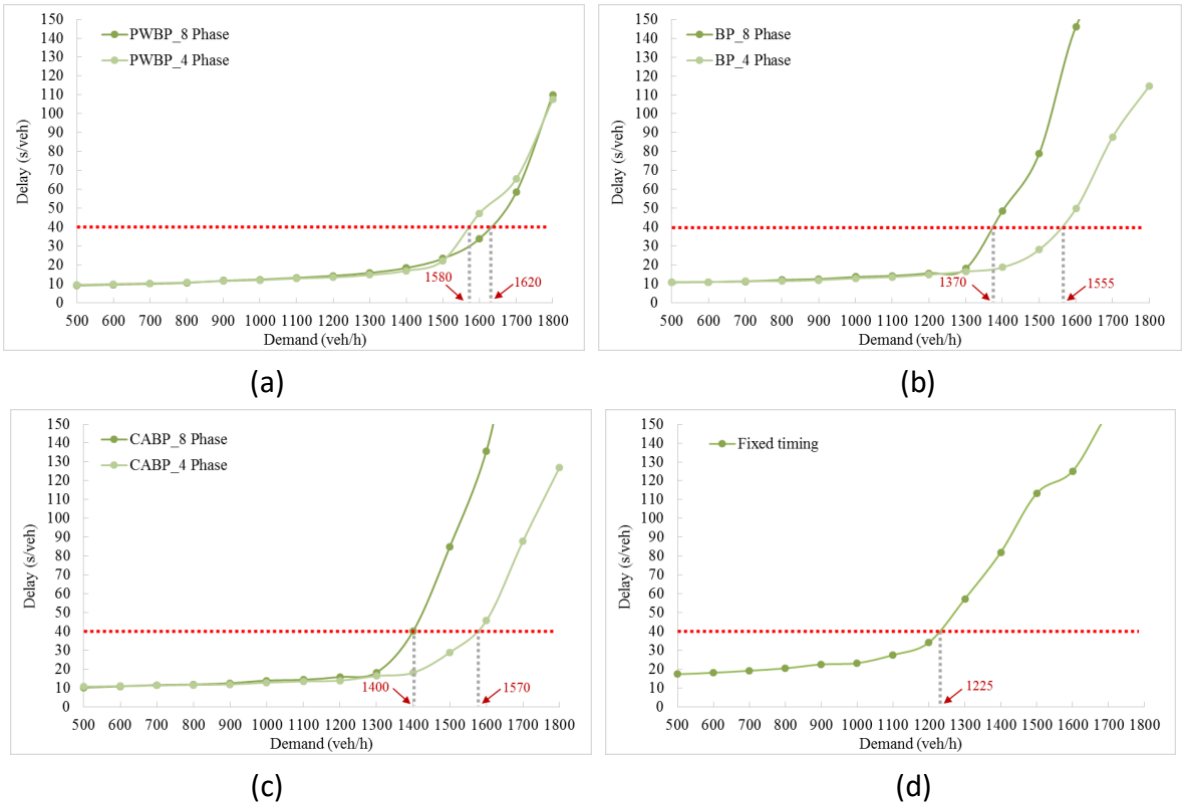

Figure 5-20 Delay patterns at varying demand levels for different control policies.

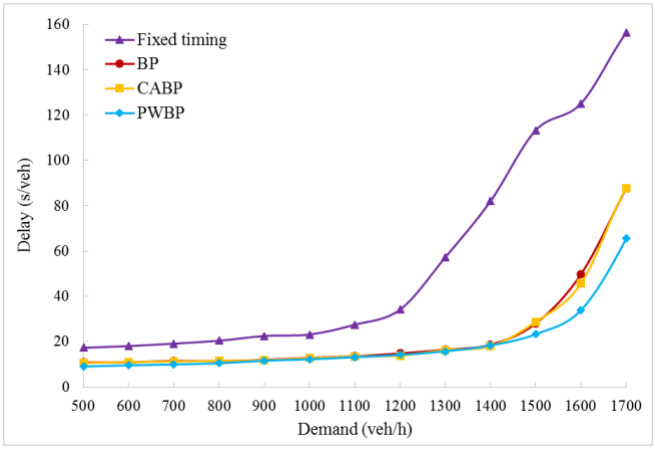

Figure 5-21 Network delays associated with different control policies.

5.2.3 Congestion propagation

In the following experiments, we set the demand levels to the deterioration bounds of the control policies and compare how congestion levels propagate over time. Since the deterioration bounds for BP and CABP are close, we just use CABP's bound (1570 veh/h); we, hence, compare three demand scenarios. Figure 5-22 and Figure 5-23 show how the speeds of all vehicles within the network are distributed under demand levels 1225, 1570 and 1620 veh/h. The horizontal axes in these figures are time and the vertical axes are percentage of vehicles traveling at or below the color-coded speeds. Under the different demand levels, the network eventually becomes grid-locked (at different levels for the different control policies). Specifically, it takes about four hours until total network gridlock under a fixed timing plan when the demand reaches 1225 veh/h, under BP and CABP it takes approximately six hours (at 1570 veh/h) until gridlock, and for PWBP, it takes approximately seven hours. This indicates that PWBP is more resilient than the other policies. Figure 5-24 shows how the total number of vehicles (stuck) in the network evolves with time.

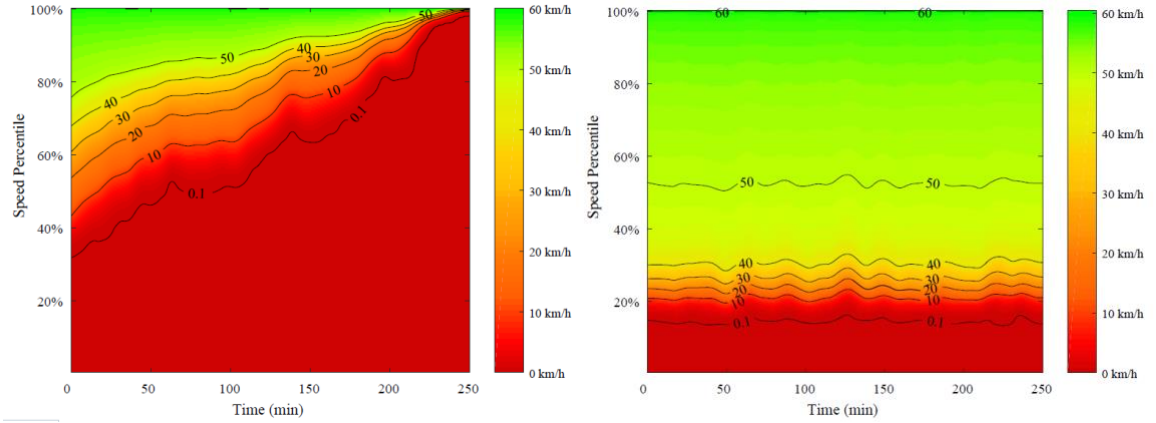

(a) FT@1225vph

(b) BP@1225vph

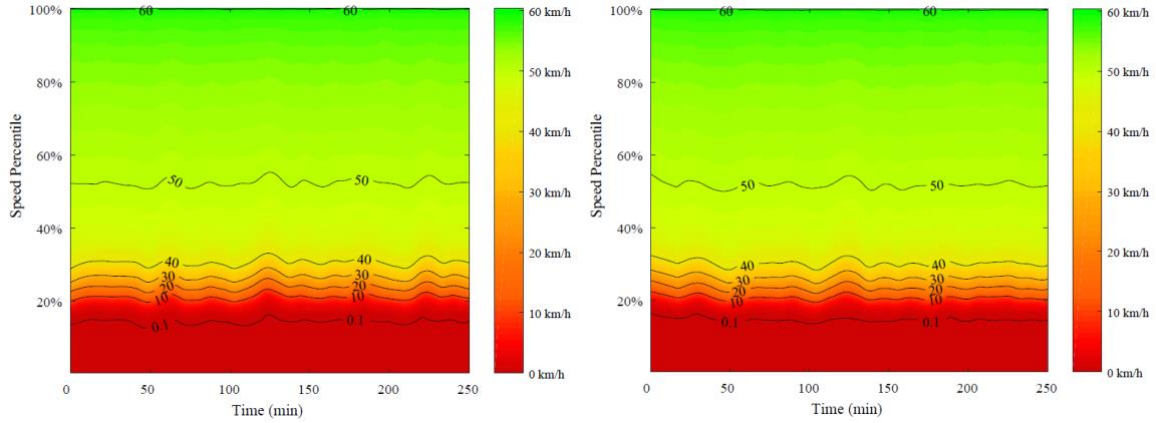

(c) CABP@1225vph

(d) PWBP@1225vph

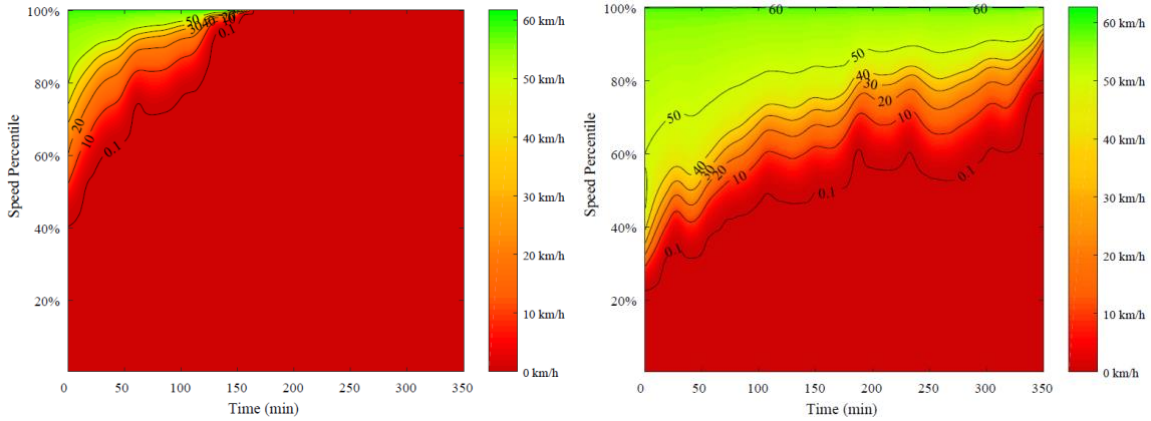

(e) FT@1570vph (f) BP@1570vph

Figure 5-22 Network speed evolution, (a) fixed timing under a demand level of 1225 veh/h, (b) BP under a demand level of 1225 veh/h, (c) CABP under a demand level of 1225 veh/h, and (d) PWBP under a demand level of 1225 veh/h, (e) fixed timing under a demand level of 1570 veh/h, (f) BP under a demand level of 1570 veh/h.

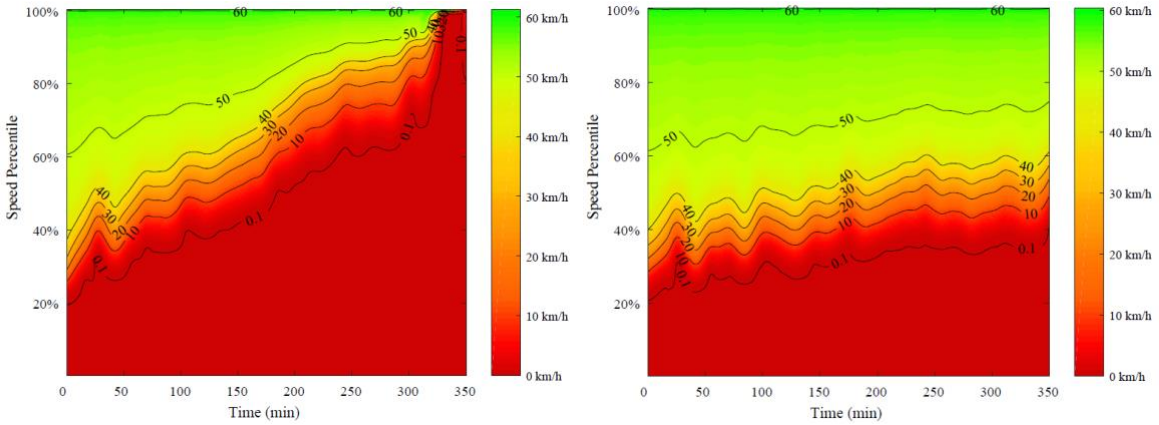

(a) CABP@1570vph (b) PWBP@1570vph

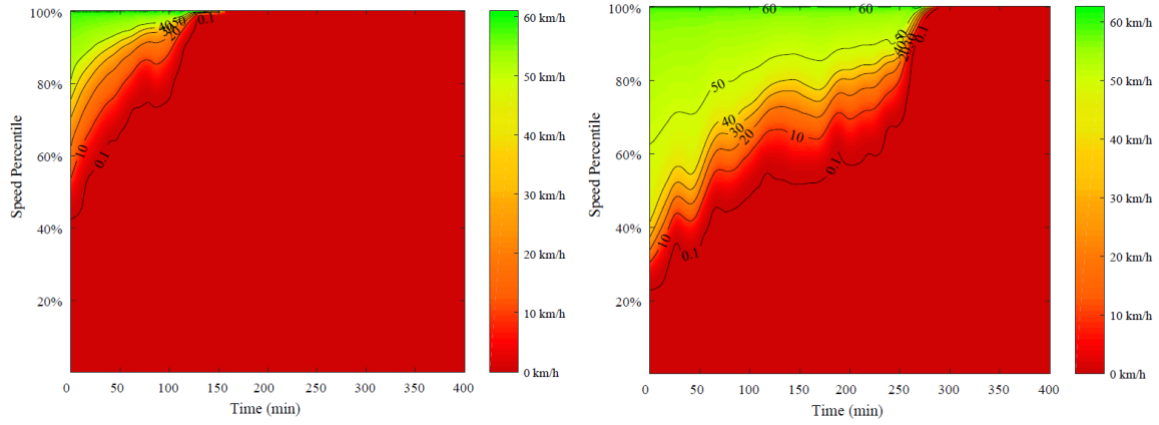

(c) FT@1620vph (d) BP@1620vph

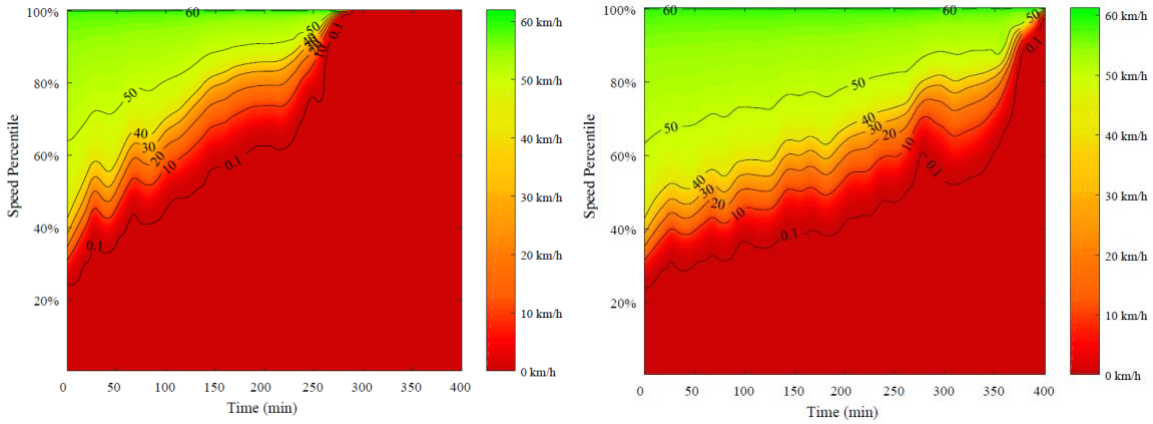

(e) CABP@1620vph (f) PWBP@1620vph

Figure 5-23 Network speed evolution, (a) CABP under a demand level of 1570 veh/h, (b) PWBP under a demand level of 1570 veh/h, (c) fixed timing under a demand level of 1620 veh/h, and (d) BP under a demand level of 1620 veh/h, (e) CABP under a demand level of 1620 veh/h, (f) PWBP under a demand level of 1620 veh/h.

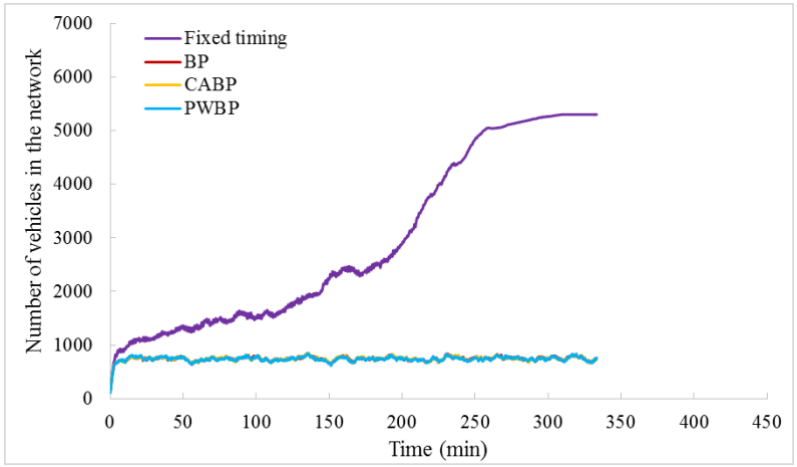

(a)

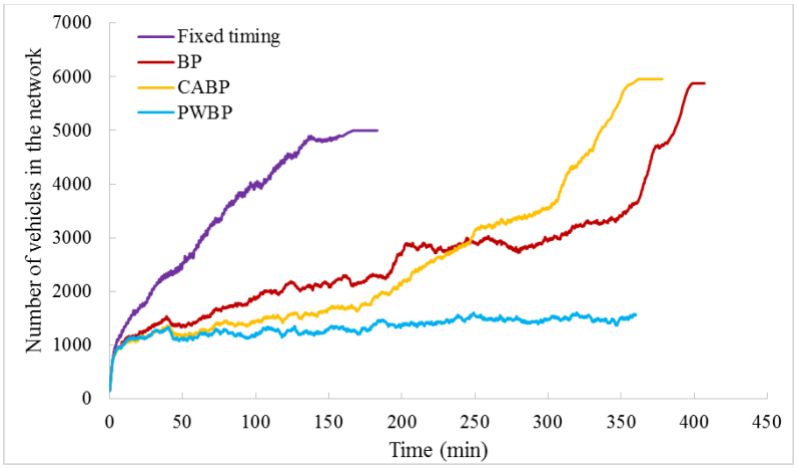

(b)

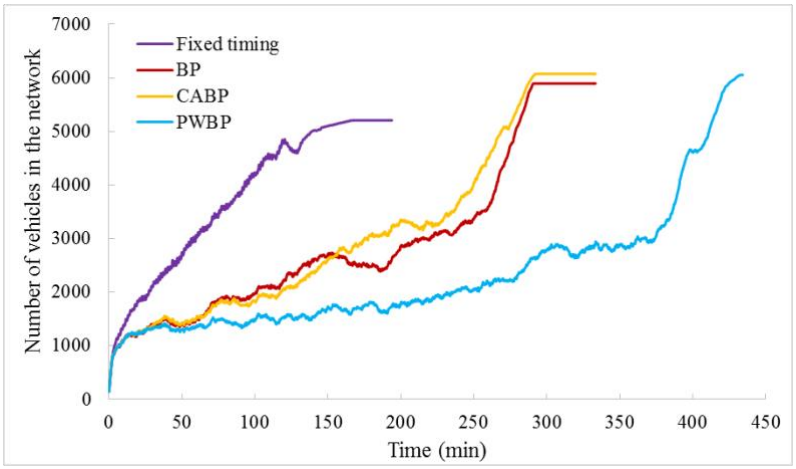

(c)

Figure 5-24 Evolution of total numbers vehicles in the network under different control policies and demand levels of (a) 1225 veh/h, (b) 1570 veh/h, and (c) 1620 veh/h.

5.2.4 Recoverability from congestion

Figure 5-25 shows how different control policies recover from congestion. The total simulation time is eight hours, the time interval from t = 120 min to t = 240 min is set as a congested period, during which demand levels are set to the deterioration bounds. We set a demand of 1000 veh/h for the remainder of the eight-hour simulation time. Figure 5-25a, b and c only differ in the demand levels during the congested period. The congested period demand levels are 1225, 1570 and 1620 veh/h in Figure 5-25a, b and c, respectively. According to Figure 5-25, for all tested scenarios, PWBP outperforms the other three control policies in terms of both delay and recovery time. Even when the peak demand reaches 1620 veh/h, PWBP only needs 30 min to recover from the congestion, while fixed timing needs about 90 min to recover with a peak demand of 1225 veh/h. Note that when the peak demand reaches 1570 and 1620 veh/h, the delay levels under fixed timing becomes too high and hence cannot be shown in Figure 5-25b and c. We also see that using fixed timing, the network does not eventually recover from congestion.

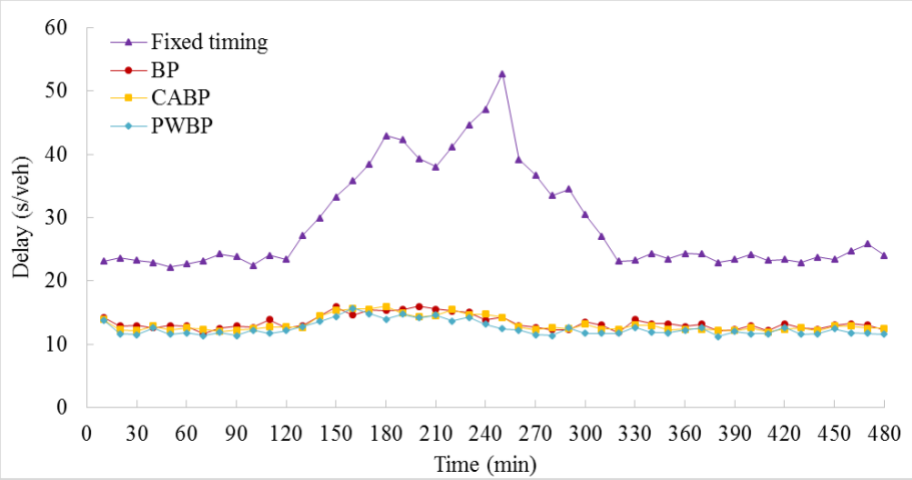

(a) demand@1225vph

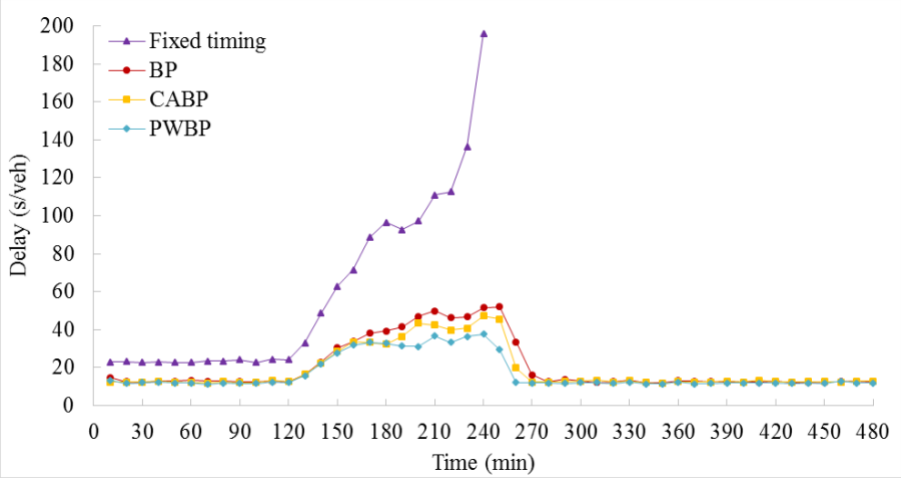

(b) demand@1570vph

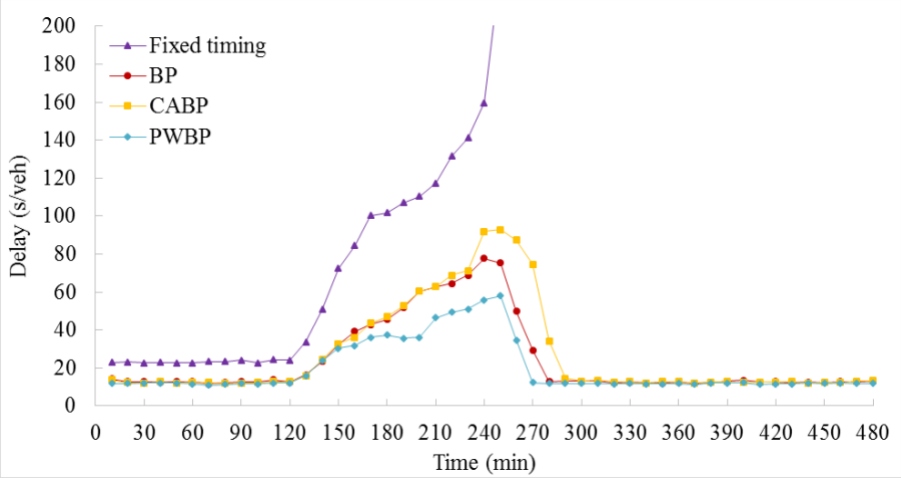

(c) demand@1620vph

Figure 5-25 Average network delay under varying peak period demands.

5.2.5 Response to an incident

We investigate the performance of PWBP in the presence of an incident located at the yellow spot in Figure 5-19. The incident is located half-way between intersections A and B, along a 3-lanes arc. We test scenarios where one lane and two lanes are blocked for a duration of one and two hours, and under different demand levels. Figure 5-26 shows the results for one-lane blocked cases when demand is 1500 veh/h. Fixed timing is not included here since 1500 veh/h is beyond its capacity region and the delays will only increase without bound. Dotted lines represent the non-incident cases, while dashed and solid lines represent the incident cases with one and two hour durations, respectively. The incident starts at the 60th min in both cases. When the incident duration is one hour, we see that the network recovers within 30 minutes after the incident is cleared under BP, CABP and PWBP. However, when the incident duration is two hours, PWBP only needs one hour to completely recover, while congestion in the network persists for significantly longer under BP and CABP: the effects of the incident are still felt in the network three hours after the incident is cleared (compared to the no-incident scenarios).

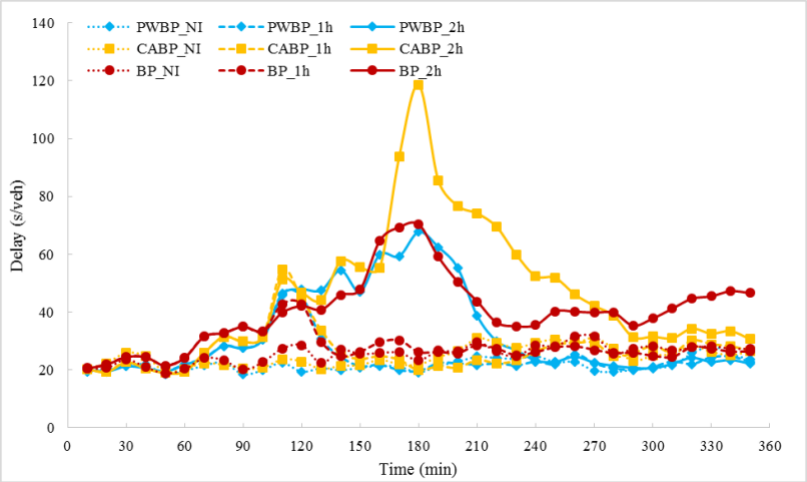

Figure 5-26 Delays associated with different policies with one lane blocked by the incident under a demand level of 1500 veh/h.

Figure 5-27 shows the two-lanes-blocked cases when demand is 1200 veh/h. The network fails to recover under fixed timing, BP and CABP control when the incident blocks two of the three lanes. The delays increase sharply and the whole network becomes gridlocked. In contrast, using PWBP control the incident hardly has any impact at all on network delay.

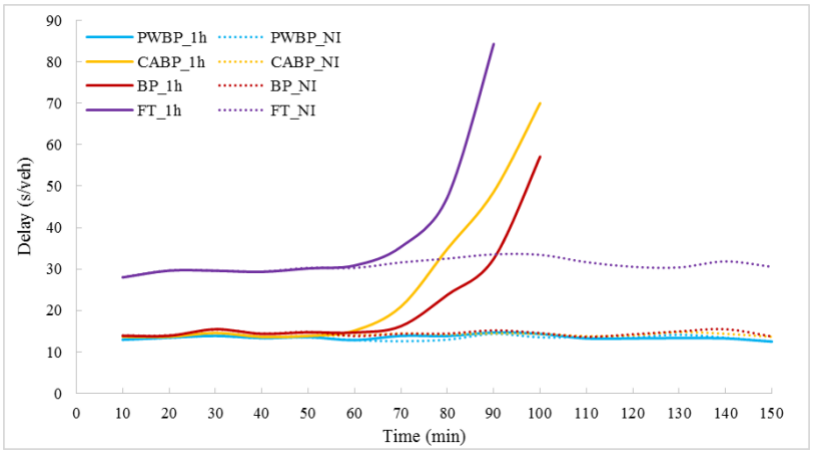

Figure 5-27 Delays associated with different policies with two lanes blocked by the incident under a demand level of 1200 veh/h.

The reason for the performance difference between BP, CABP and PWBP originates from how the model deals with scenarios in Figure 1-1b and Figure 1-1c. With an incident located half-way between intersections A to B, the incident results in congested conditions (queueing) between the incident location and intersection A and low volume traffic between incident location and intersection B. When the queue spills back to intersection A (similar to Figure 1-1b), PWBP will forbid the movements from A to B, while BP and CABP fail to capture the spillback dynamics. In addition, PWBP does not allocate green time at intersection B to the movement from A when there are actually no vehicle near the stop line (similar to Figure 1-1c), while BP and CABP may still allocate green time to this movement.

6 Conclusion and outlook

This research builds a calibrated simulation network based on field data from Abu Dhabi, and uses machine learning to develop a SCOOT emulator. The trained SCOOT emulator is compared with the actual SCOOT system and results show high accuracy of the emulator.

We study two methodologies for traffic state estimation. One uses random fields to learn traffic flow dynamics, and the other one uses stochastic Lagrangian dynamics to estimate traffic states. The former combines mesoscopic traffic modeling with the statistical power of probabilistic graphical models to learn the traffic patterns from historical data, and the modeling approach includes both look-ahead dynamics along with vehicle interaction dynamics. A conditional random fields (CRF) approach using a factor graph representation of the dynamics is then proposed for purposes of statistical learning when limited data is available. Coverage of the probe vehicle information can be expected to be highly random as well as sparse in the real-world. The experiments demonstrate that the distribution of probes in a sample can severely impact the estimation results, and hence it is not sufficient to specify adequate penetration levels with a single value. The latter adopts the Newell-Franklin speed-spacing relation and introduced stochasticity via parametric uncertainties. An ensemble averaged process is derived, which is consistent with traditional first-order Godunov schemes using a mean speed-spacing relation (as numerical flux), not a traditional equilibrium relation. The mean process is shown to converge to a conservation law in Lagrangian coordinates. We then derive the covariance dynamics of the model by applying a Gaussian approximation. We provide two experiments to demonstrate the estimation capability of the proposed approach for more realistic settings. In the first experiment we use vehicle trajectory data from a calibrated microscopic traffic simulation model of an arterial road in Ann Arbor City in Michigan. The estimation results show that traffic states, in terms of speed and density dynamics, can be well captured when the penetration rate increase to 20%. In the second experiment, we use NGSIM trajectory data along I-80 in the San Francisco Bay area in Emeryville, CA. The traffic state in terms of density dynamics can be well estimated with 10% penetration rate. The investigation of the speed estimation error in terms of RMSEs for different penetration rates illustrate that there is strong improvement as the penetration rates increase from 5% to 15%.

For traffic control, we propose a backpressure-based technique that is based on macroscopic traffic flow, which we refer to as position-weighted backpressure (PWBP). PWBP considers the

spatial distribution of vehicles when calculating the backpressure weights. The PWBP control policy is tested using a microscopic traffic simulation model of an eleven-intersection network in Abu Dhabi. Comparisons against coordinated and optimized fixed signal timing, standard BP, and a capacity-aware variant of BP (CABP) were carried out. The results indicate that PWBP can accommodate higher demand levels than the other three control policies and outperforms them in terms of total network delay, congestion propagation speed, recoverability from heavy congestion, and response to an incident.

One of the drawbacks of the proposed random field estimation approach is: as the traffic state predicted at each time-step becomes the input vector for the following estimation model, errors in the state estimates propagate with time. This drawback can be addressed using spatio-temporal graphical representations, but the factor graphs in such a setting along with the associated learning models can be very challenging from a computational stand-point. The model can also be extended to multi-lane roads, and the CRF models can be improved by adopting higher order Markov models to capture the influence of vehicles further downstream (ahead of the leader), which could yield higher estimation accuracy with lower probe penetration rates. The computational issues are not suffered by the Lagrangian state estimation approach, which develops a macroscopic model based on car-following theory and a Gaussian approximation for quick estimation using standard Kalman filters.

As to the PWBP control policy, this research has focused on prioritization of movements at network intersections. As a possible future research direction, this can be extended to include real-time route guidance.

7 References

1. Yuan, Y., et al. "Real-time Lagrangian traffic state estimator for freeways." *IEEE Transactions on Intelligent Transportation Systems* 13:1 (2012), pp. 59-70.
2. Seo, T. and Takahiko, K. "Probe vehicle-based traffic state estimation method with spacing information and conservation law." *Transportation Research Part C* 59 (2015), pp. 391-403.
3. Hofleitner, A., Herring, R., Abbeel, P. and Bayen, A. "Learning the dynamics of arterial traffic from probe data using a dynamic Bayesian network." *IEEE Transactions on Intelligent Transportation Systems* 13:4 (2012), pp. 1679-1693.
4. Herrera, J.C. and Alexandre, M.B. "Incorporation of Lagrangian measurements in freeway traffic state estimation." *Transportation Research Part B* 44:4 (2010), pp. 460-481.
5. Jabari, S.E. and Henry, X.L. "A stochastic model of traffic flow: Theoretical foundations." *Transportation Research Part B* 46:1 (2012), pp. 156-174.
6. Jabari, S.E. and Henry, X.L. "A stochastic model of traffic flow: Gaussian approximation and estimation." *Transportation Research Part B* 47 (2013), pp. 15-41.
7. Deng, W., Hao, L. and Xuesong, Z. "Traffic state estimation and uncertainty quantification based on heterogeneous data sources: A three detector approach." *Transportation Research Part B* 57 (2013), pp. 132-157.
8. Work, D.B., et al. "An ensemble Kalman filtering approach to highway traffic estimation using GPS enabled mobile devices." *Decision and Control, 2008. CDC 2008. 47th IEEE Conference on*. IEEE, (2008), pp. 5062-5068.
9. Hellinga, B., Izadpanah, P., Takada, H. and Fu, L. "Decomposing travel times measured by probe-based traffic monitoring systems to individual road segments." *Transportation Research Part C* 16:6 (2008), pp. 768-782.
10. Chen, H. and Hesham, A.R. "Prediction of dynamic freeway travel times based on vehicle trajectory construction." *Intelligent Transportation Systems (ITSC), 2012 15th International IEEE Conference on*. IEEE, 2012.
11. Hunter, T., et al. "Large Scale Estimation in Cyberphysical Systems using Streaming Data: a Case Study with Smartphone Traces." *arXiv preprint arXiv:1212.3393*(2012).
12. Jenelius, E., and Haris, N. K. "Urban network travel time prediction based on a probabilistic principal component analysis model of probe data." *IEEE Transactions on Intelligent Transportation Systems* 19:2 (2018), pp. 436-445.
13. Dilip, D.M., Nikolaos, M.F. and Jabari, S.E. *Sparse Estimation of Travel Time Distributions Using Gamma Kernels*. No. 17-02971. 2017.

14. Jabari, S.E., Nikolaos, M.F. and Deepthi, M.D. "Sparse travel time estimation from streaming data." *arXiv preprint arXiv:1804.08130* (2018).
15. Herring, R., et al. "Estimating arterial traffic conditions using sparse probe data." *Intelligent Transportation Systems (ITSC), 2010 13th International IEEE Conference on*. IEEE, 2010.
16. Hofleitner, A., Ryan, H. and Alexandre, B. "Arterial travel time forecast with streaming data: A hybrid approach of flow modeling and machine learning." *Transportation Research Part B* 46:9 (2012), pp. 1097-1122.
17. Papathanasopoulou, V. and Constantinos, A. "Towards data-driven car-following models." *Transportation Research Part C* 55 (2015), pp. 496-509.
18. Furtlehner, C., Jean-Marc, L. and Arnaud de, L.F. "A belief propagation approach to traffic prediction using probe vehicles." *10th International IEEE Conference on Intelligent Transportation Systems*. 2007.
19. Vandenberghe, W., et al. "Feasibility of expanding traffic monitoring systems with floating car data technology." *IET Intelligent Transport Systems* 6:4 (2012), pp. 347-354.
20. Jabari, S.E. and Laura, W. "Sensor placement with time-to-detection guarantees." *EURO Journal on Transportation and Logistics* 5:4 (2016), pp. 415-433.
21. Mazaré, P., et al. "Trade-offs between inductive loops and GPS probe vehicles for travel time estimation: A Mobile Century case study." *Transportation Research Board 91st Annual Meeting (TRB'12)*. Vol. 349. 2012.
22. Hiribarren, G. and Juan, C.H. "Real time traffic states estimation on arterials based on trajectory data." *Transportation Research Part B* 69 (2014), pp. 19-30.
23. Ban, X.J., et al. "Delay pattern estimation for signalized intersections using sampled travel times." *Transportation Research Record* 2130:1 (2009), pp. 109-119.
24. Ban, X.J., Peng, H. and Zhanbo, S. "Real time queue length estimation for signalized intersections using travel times from mobile sensors." *Transportation Research Part C* 19:6 (2011), pp. 1133-1156.
25. Zheng, F., Saif, E.J., Henry, X.L. and Dianchao, L. "Traffic state estimation using stochastic Lagrangian dynamics." *Transportation Research Part B 115* (2018), pp. 143-165.
26. Kim, S. and Benjamin, C. "Comparing INRIX speed data against concurrent loop detector stations over several months." *Transportation Research Part C* 49 (2014), pp. 59-72.
27. Bar-Gera, H. "Evaluation of a cellular phone-based system for measurements of traffic speeds and travel times: A case study from Israel." *Transportation Research Part C* 6 (2007), pp. 380-391.
28. Lighthill, M.J. and Whitham, G.B. "On kinematic waves I. Flood movement in long rivers." *Proc. R. Soc. Lond. A* 229:1178 (1955), pp. 281-316.

29. Richards, P. "Shock waves on the highway." *Operations research* 4:1 (1956), pp. 42-51.
30. Daganzo, C.F. "A variational formulation of kinematic waves: basic theory and complex boundary conditions." *Transportation Research Part B* 39:2 (2005), pp. 187-196.
31. Daganzo, C.F. "A variational formulation of kinematic waves: Solution methods." *Transportation Research Part B* 39:10 (2005), pp. 934-950.
32. Leclercq, L., Jorge, A.L. and Estelle, C. "The Lagrangian coordinates and what it means for first order traffic flow models." *Transportation and Traffic Theory* (2007), pp. 735–753.
33. Claudel, C.G. and Alexandre, M.B. "Lax–Hopf based incorporation of internal boundary conditions into Hamilton–Jacobi equation. Part I: Theory." *IEEE Transactions on Automatic Control* 55:5 (2010), pp. 1142-1157.
34. Friesz, T.L., et al. "Dynamic user equilibrium based on a hydrodynamic model." *Transportation Research Part B* 47 (2013), pp. 102-126.
35. Laval, J.A. and Ludovic, L. "The Hamilton–Jacobi partial differential equation and the three representations of traffic flow." *Transportation Research Part B* 52 (2013), pp. 17-30.
36. Duret, A. and Yufei, Y. "Traffic state estimation based on Eulerian and Lagrangian observations in a mesoscopic modeling framework." *Transportation research part B* 101 (2017), pp. 51-71.
37. Daganzo, C.F. "The cell transmission model: A dynamic representation of highway traffic consistent with the hydrodynamic theory." *Transportation Research Part B* 28:4 (1994), pp. 269-287.
38. Daganzo, C.F. "The cell transmission model, part II: network traffic." *Transportation Research Part B* 29:2 (1995), pp. 79-93.
39. Sumalee, A., et al. "Stochastic cell transmission model (SCTM): A stochastic dynamic traffic model for traffic state surveillance and assignment." *Transportation Research Part B* 45:3 (2011), pp. 507-533.
40. Yperman, I. "The link transmission model for dynamic network loading." (2007).
41. Osorio, C., Gunnar, F. and Michel, B. "Dynamic network loading: a stochastic differentiable model that derives link state distributions." *Procedia-Social and Behavioral Sciences* 17 (2011), pp. 364-381.
42. Osorio, C. and Gunnar, F. "Capturing dependency among link boundaries in a stochastic dynamic network loading model." *Transportation Science* 49:2 (2014), pp. 420-431.
43. Osorio, C. and Carter, W. "On the analytical approximation of joint aggregate queue-length distributions for traffic networks: A stationary finite capacity Markovian network approach." *Transportation Research Part B* 95 (2017), pp. 305-339.

44. Lu, J. and Carolina, O. "A probabilistic traffic-theoretic network loading model suitable for large-scale network analysis." *Transportation Science* (2018).
45. Seo, T., et al. "Traffic state estimation on highway: A comprehensive survey." *Annual Reviews in Control* 43 (2017), pp. 128-151.
46. Wang, R., Yanning, L. and Daniel, B.W. "Comparing traffic state estimators for mixed human and automated traffic flows." *Transportation Research Part C* 78 (2017), pp. 95-110.
47. Gazis, D.C. and Charles, H. K. "On-line estimation of traffic densities from time-series of flow and speed data." *Transportation Science* 5:3 (1971), pp. 283-301.
48. Szeto, M.W. and Denos, C.G. "Application of Kalman filtering to the surveillance and control of traffic systems." *Transportation Science* 6:4 (1972), pp. 419-439.
49. Muñoz, L., et al. "Traffic density estimation with the cell transmission model." *American Control Conference, 2003. Proceedings of the IEEE* 2003:5. (2003), pp. 3750–3755.
50. Gazis, D and Chiu, L. "Kalman filtering estimation of traffic counts for two network links in tandem." *Transportation Research Part B* 37:8 (2003), pp. 737-745.
51. Wang, Y. and Markos, P. "Real-time freeway traffic state estimation based on extended Kalman filter: a general approach." *Transportation Research Part B* 39:2 (2005), pp. 141-167.
52. Boel, R. and Lyudmila, M. "A compositional stochastic model for real time freeway traffic simulation." *Transportation Research Part B* 40:4 (2006), pp. 319-334.
53. Wang, Y., Markos, P. and Albert, M. "Real-time freeway traffic state estimation based on extended Kalman filter: A case study." *Transportation Science* 41:2 (2007), pp. 167-181.
54. Di, X., Henry, L. and Gary, D. "Hybrid Extended Kalman Filtering Approach for Traffic Density Estimation Along Signalized Arterials: Use of Global Positioning System Data." *Transportation Research Record: Journal of the Transportation Research Board* 2188 (2010), pp. 165-173.
55. Blandin, S., Couque, A., Bayen, A. and Work, D. "On sequential data assimilation for scalar macroscopic traffic flow models." *Physica D: Nonlinear Phenomena* 241:17 (2012), pp. 1421-1440.
56. Yuan, Y., Aurélien, D. and Hans, V.L. "Mesoscopic traffic state estimation based on a variational formulation of the LWR model in Lagrangian-space coordinates and Kalman filter." *Transportation Research Procedia* 10 (2015), pp. 82-92.
57. Chu, K., Romesh, S. and Kazuhiro, S. "Stochastic Lagrangian Traffic flow modeling and real-time traffic prediction." *Automation Science and Engineering (CASE), 2016 IEEE International Conference on*. IEEE, 2016.

58. Jabari, S.E., Jianfeng, Z. and Henry, X.L. "A probabilistic stationary speed–density relation based on Newell's simplified car-following model." *Transportation Research Part B* 68 (2014), pp. 205-223.
59. Newell, G.F. "Nonlinear effects in the dynamics of car following." *Operations research* 9:2 (1961), pp. 209-229.
60. Del Castillo, J.M. and Benitez, F. G. "On the functional form of the speed-density relationship—I: General theory." *Transportation Research Part B* 29:5 (1995), pp. 373-389.
61. Newell, G.F. "A simplified car-following theory: a lower order model." *Transportation Research Part B* 36:3 (2002), pp. 195-205.
62. Dujardin, Y., et al. "Multiobjective and multimodal adaptive traffic light control on single junctions." *Intelligent Transportation Systems (ITSC), 2011 14th International IEEE Conference on*. IEEE, (2011), pp. 1361–1368.
63. Gartner, N. H. *OPAC: A demand-responsive strategy for traffic signal control*. No. 906. 1983.
64. Tettamanti, T. and István, V. "Distributed traffic control system based on model predictive control." *Periodica Polytechnica Civil Engineering* 54:1 (2010), pp. 3-9.
65. Mirchandani, P. and Larry, H. "A real-time traffic signal control system: architecture, algorithms, and analysis." *Transportation Research Part C* 9:6 (2001), pp. 415-432.
66. You, X., Li, L. and Wanjing, M. "Coordinated optimization model for signal timings of full continuous flow intersections." *Transportation Research Record: Journal of the Transportation Research Board* 2356 (2013), pp. 23-33.
67. Ma, W., et al. "Coordinated optimization of signal timings for intersection approach with presignals." *Transportation Research Record: Journal of the Transportation Research Board* 2355 (2013), pp. 93-104.
68. Cervero, R. "Unlocking suburban gridlock." *Journal of the American Planning Association* 52:4 (1986), pp. 389-406.
69. Heung, T.H., Tin, K.H. and Yu, F.F. "Coordinated road-junction traffic control by dynamic programming." *IEEE Transactions on Intelligent Transportation Systems* 6:3 (2005), pp. 341-350.
70. Gettman, D., et al. "Data-driven algorithms for real-time adaptive tuning of offsets in coordinated traffic signal systems." *Transportation Research Record* 2035:1 (2007), pp. 1-9.
71. Papageorgiou, M., et al. "Review of road traffic control strategies." *Proceedings of the IEEE* 91:12 (2003), pp. 2043-2067.
72. Smith, M.J. "A local traffic control policy which automatically maximises the overall travel capacity of an urban road network." *Traffic Engineering & Control* 21.HS-030 129 (1980).

73. Lämmer, S. and Dirk, H. "Self-control of traffic lights and vehicle flows in urban road networks." *Journal of Statistical Mechanics: Theory and Experiment* 2008:04 (2008), P04019.
74. Lämmer, S. and Dirk, H. "Self-stabilizing decentralized signal control of realistic, saturated network traffic." Santa Fe Institute, 2010.
75. Smith, M. "Dynamics of route choice and signal control in capacitated networks." *Journal of Choice Modelling* 4:3 (2011), pp. 30-51.
76. Wongpiromsarn, T., et al. "Distributed traffic signal control for maximum network throughput." *Intelligent Transportation Systems (ITSC), 2012 15th International IEEE Conference on*. IEEE, (2012), pp. 588–595.
77. Varaiya, P. "Max pressure control of a network of signalized intersections." *Transportation Research Part C* 36 (2013), pp. 177-195.
78. Xiao, N., et al. "Pressure releasing policy in traffic signal control with finite queue capacities." *Decision and Control (CDC), 2014 IEEE 53rd Annual Conference on*. IEEE, (2014), pp. 6492–6497.
79. Le, T., et al. "Decentralized signal control for urban road networks." *Transportation Research Part C* 58 (2015), pp. 431-450.
80. De Gier, J., Timothy, M.G., and Omar, R. "Traffic flow on realistic road networks with adaptive traffic lights." *Journal of Statistical Mechanics: Theory and Experiment* 2011:04 (2011): P04008.
81. Tassiulas, L. and Anthony, E. "Stability properties of constrained queueing systems and scheduling policies for maximum throughput in multihop radio networks." *IEEE transactions on automatic control* 37:12 (1992), pp. 1936-1948.
82. Neely, M.J., Eytan, M. and Charles, E.R. "Dynamic power allocation and routing for time-varying wireless networks." *IEEE Journal on Selected Areas in Communications* 23:1 (2005), pp. 89-103.
83. Georgiadis, L., Michael, J.N. and Leandros, T. "Resource allocation and cross-layer control in wireless networks." *Foundations and Trends® in Networking* 1:1 (2006), pp. 1-144.
84. Neely, M.J. "Stochastic network optimization with application to communication and queueing systems." *Synthesis Lectures on Communication Networks* 3:1 (2010), pp. 1-211.
85. Gregoire, J., et al. "Capacity-aware backpressure traffic signal control." *IEEE Transactions on Control of Network Systems* 2:2 (2015), pp. 164-173.
86. Hunt, P.B., Robertson, D.I., Bretherton, R.D. and Royle, M.C. “The SCOOT on-line traffic signal optimisation technique”, *Traffic Engineering & Control*, 23:4, (1982). pp. 190-192.
87. Abu Dhabi Department of Transport (AD DoT), https://www.dot.abudhabi.ae/en/home.

88. Bishop, C.M. "Pattern recognition and machine learning (information science and statistics) springer-verlag new york." *Inc. Secaucus, NJ, USA* (2006).
89. Goodfellow, I., et al. *Deep learning*. Vol. 1. Cambridge: MIT press, 2016.
90. Recurrent Neural Network Tutorial, http://www.wildml.com/2015/09/recurrent-neural-networks-tutorial-part-1-introduction-to-rnns/.
91. Hochreiter, S. and Jürgen, S. "Long short-term memory." *Neural computation* 9:8 (1997), pp.1735-1780.
92. Python programming language, https://www.python.org/.
93. TensorFlow, https://www.tensorflow.org/.
94. Fellendorf, M. and Peter, V. "Microscopic traffic flow simulator VISSIM." *Fundamentals of traffic simulation*. Springer, New York, NY, (2010), pp. 63-93.
95. Component Object Model (COM), https://en.wikipedia.org/wiki/Component_Object_Model.
96. Synchro Studio - Trafficware Group Inc., http://www.trafficware.com/synchro.html.
97. Sopasakis, A. and Markos A. K. "Stochastic modeling and simulation of traffic flow: asymmetric single exclusion process with Arrhenius look-ahead dynamics." *SIAM Journal on Applied Mathematics* 66:3 (2006), pp. 921-944.
98. Lárraga, M.E., Del Rio, J. A. and Alvarez-Lcaza, L. "Cellular automata for one-lane traffic flow modeling." *Transportation Research Part C* 13:1 (2005), pp. 63-74.
99. Jerath, K., et al. "Statistical mechanics-inspired framework for studying the effects of mixed traffic flows on highway congestion." *American Control Conference (ACC), 2014*. IEEE, 2014.
100. Jerath, K., et al. "Dynamic prediction of vehicle cluster distribution in mixed traffic: a statistical mechanics-inspired method." *IEEE Transactions on Intelligent Transportation Systems* 16:5 (2015), pp. 2424-2434.
101. Jabari, S.E. "Node modeling for congested urban road networks." *Transportation Research Part B* 91 (2016), pp. 229-249.
102. Koller, D. and Nir, F. *Probabilistic graphical models: principles and techniques*. MIT press, 2009.
103. Bishop, C.M. "Periodic Variables." *Pattern recognition and machine learning* 1 (2006).
104. Bucknell, C. and Juan, C.H. "A trade-off analysis between penetration rate and sampling frequency of mobile sensors in traffic state estimation." *Transportation Research Part C* 46 (2014), pp. 132-150.
105. Goodall, N.J., Brian, L.S. and Byungkyu, B.P. "Microscopic estimation of freeway vehicle positions from the behavior of connected vehicles." *Journal of Intelligent Transportation Systems* 20:1 (2016), pp. 45-54.